ALPHEUS

Multidisciplinary optimized PD design

D2.4.

Grant Agreement No.	883553
Start date of Project	01-04-2020
Duration of the Project	48 months
Deliverable Number	D2.4
Deliverable Leader	NTNU
Dissemination Level	Public
Version	V2.0
Submission Date	30-06-2023
Authors	Luiz Henrique Accorsi Gans, NTNU Pål-Tore Selbo Storli, NTNU

This project has received funding from the European Union's Horizon 2020 research and innovation programme under grant agreement No 883553.

Modification Control

Version #	Description	Author	Organisation	Date
0.1	First version based on D2.5, CFD validation and design optimization description	Luiz Henrique Accorsi Gans	NTNU	29-11-2022
0.2	Revised version	Luiz Henrique Accorsi Gans Pål-Tore Selbo Storli	NTNU	30-11-2022
1.0	Final version	Luiz Henrique Accorsi Gans Pål-Tore Selbo Storli	NTNU	30-11-2022
1.1	First draft to revised version	Luiz Henrique Accorsi Gans Pål-Tore Selbo Storli	NTNU	12-06-2023
1.2	Revised version	Luiz Henrique Accorsi Gans Pål-Tore Selbo Storli	NTNU	19-06-2023
1.3	Revised version	Luiz Henrique Accorsi Gans Pål-Tore Selbo Storli	NTNU	26-06-2023
2.0	Final revised version	Luiz Henrique Accorsi Gans Pål-Tore Selbo Storli	NTNU	30-06-2023

Release Approval

Name	Role	Date
H. Nilsson	WP Leader	30-06-2023
J. Bricker	Scientific Project Coordinator (TU Delft)	30-06-2023
J.R. Moll	Executive Project Coordinator (TU Delft)	30-06-2023

Table of Contents

List of figures

List of tables

1 Executive Summary

This report presents the work and conclusions regarding the multidisciplinary optimization of a positive displacement reversible pump-turbine (PD RPT) machine. Both an analytical and numerical model of such a PD RPT is made, analysed for 10 MW scale and laboratory scale, respectively.

The analytical model is partially verified and includes fish mortality and the subsequent effect on main dimensions if fish mortality is given a cost. The conclusion is that a PD RPT is likely not to be a fish friendly energy storage machine for the longer (>~1m) fish species found in coastal regions.

The numerical model is validated using high-fidelity experimental results and is used to optimize the laboratory scale test rig that will be manufactured and experimentally studied in the ALPHEUS project. A structural analysis of the operation of this indicates that there are no reasons for concern with respect to structural integrity and fatigue of this laboratory scale model.

2 Introduction

ALPHEUS deliverable D2.4 reports the multidisciplinary optimization of a PD RPT design performed by the ALPHEUS project. The deliverable is part of Task 2.3 “Multidisciplinary optimization of Positive Displacement RPT [M1-M24]”.

This multidisciplinary optimization follows two paths:

One is based on an analytical model of the efficiency of a PD machine, which to the authors’ knowledge is never done before. This is briefly presented in Section 3, with the full model presented in the Appendix. The analytical model is verified using Computational Fluid Dynamics (CFD) results, and the CFD model is validated using experimental results, both using classical measurement techniques for hydraulic machinery obtaining flow and head, but also using highly resolved Particle Image Velocimetry (PIV) measurement. The experimental setup is described in deliverable D2.5, but some details are repeated in Section 4, for clarity. The analytical model is linked to fish mortality and main dimensions are optimized. Section 8 of this report presents the multidisciplinary optimization where fish mortality has been included. Reducing fish mortality (increasing fish friendliness) is an important topic for the technological development carried out by ALPHEUS. Implementing fish friendliness at an early stage in a technological optimization will promote fish survival and the feasibility of low head pumped storage power plants all together. The analysis including fish mortality effectively shifts the main dimensions towards a more fish friendly design. To the authors’ knowledge such an implementation of fish friendliness in the technical design optimization has never been shown before, bridging technical and biological disciplines.

The other path is using CFD for the optimization. It starts by presenting the numerical CFD simulations and the validation with the PIV measurements that are reported in deliverable D2.5. The conclusion is that the CFD model is capturing all the key flow phenomena observed in the PIV measurements and is considered validated. This is found in Section 5.

Section 6 presents a design optimization using both outcome of the present work (optimizing gap clearances and inlet width to rotor diameter ratio using CFD) and findings from other researchers to obtain the design for the tests to be performed at TU Braunschweig. Many parameters have been studied, optimized and published by other research groups, and those outcomes are taken advantage of in the present work. Examples of external findings are: rotor surface profile, inlet shape, pipe transition, twisted rotor angle.

The CFD results are also used to execute a simplified Fluid Structure Analysis (FSI) on the rotor geometry, found in Section 7. It presents the result of a one-way Fluid Structure Analysis (FSI) performed on one rotor of the design for the tests at TU Braunschweig, at the time in the operating cycle when the global torque has been found to be highest. For this design, no indication of any cause for concern on structural integrity or fatigue is raised.

3 PD machine model and optimization through parametric study

An analytical model of a PD machine has been developed. The model includes head losses, gap flows and torques from shear forces all acting on the rotors and preventing this from supplying the ideal (loss free) power in pump mode and extracting ideal power in generating mode. The full model is presented in Appendix but is briefly introduced here as well. The Appendix includes some pictures of a PD machine which can be useful for the reader to have a look at if the reader is not familiar with the geometry of a PD machine.

The losses included are:

- Volumetric losses that leak from the high-pressure side to the low-pressure side of the machine
    - The volumetric losses occur in the gap between the rotor's lobe surfaces and the casing (tip gap), between the rotors themselves (rotor-rotor gap) and in the gaps at the rotor ends and the casing (side or end gaps). These losses are either driven by the pressure difference between high-pressure and low-pressure side, or shear forces from the rotor pulling water in the direction of rotor velocity. At some location and operating modes these flow components are in the same direction, in other cases they are opposite. In fact, shear forces sometimes move flow from low pressure to high pressure side. In this case the unit is pumping at these locations, and not being a loss per se the energy must be provided by the rotor and comes into equations with the same sign as losses.
- Head loss due to flow phenomena
    - The head losses included are from shear forces between the fluid and the rotor casing (not at gap locations which are dealt with separately as flow losses or torques opposing the movement) and high velocities in the gap resulting in a jet which eventually dissipates. In turbine mode an eddy is observed rather than a jet, but losses are modelled identical as for the jet.
- Torques acting on the rotor that tries to slow down the unit.
    - The torques included are the effect from the shear forces of the net gap flows (pressure driven and shear driven velocities might have different directions). Sometimes this gives a torque opposing the rotation, and sometimes a torque aiding the rotation. As an example, in turbine mode the shear driven flow between rotor and casing is giving a torque opposing the rotation, but the flow due to leakage from high pressure to low pressure side is contributing with a torque promoting the rotation. At low rotational speeds the net torque due to both shear and leakage might very well contribute to the rotation, whereas at higher the rotational speeds the shear flow effect will be greater than the leakage flow effect and a net torque opposing the rotation is seen.

The basis for developing the expressions for flows and torques comes from the pressure driven Couette flow case, where two parallel flat surfaces are sliding relative to each other with a fluid in-between setting up a linear velocity profile and subsequent flow, as well as a pressure gradient is setting up a parabolic velocity profile in the direction of decreasing pressure, also carrying a flow. These two velocity profiles are easy to work with, both integrating to find the flow and differentiating to find the velocity gradients at surfaces to identify shear forces and torques, in case of rotating motion. These velocity profiles are implying laminar flow, which is rarely the case in practical applications. The more realistic velocity profiles are turbulent and are not so easy to work with analytically. For the work presented here a one-seventh power velocity profile is assumed and has been integrated to find the flow and approximated to find the velocity gradient. Factors for multiplication of the laminar flow values to get the one-seventh power law values has been found, and the analytical expressions in the model has been corrected using these factors. The same has been done for the velocity gradients, where correction factors are multiplied to obtain the one-seventh power law values obtaining more appropriate representation of shear forces and torques.

The optimization through parametric study is performed by setting an ideal (loss free) hydraulic power available at a specified head, in this case a prototype scale at 10 MW at 10m head. This power is used to find the dimensions of a unit based on the two parameters rotor height Z and rotational speed rps. In this way, the unit for a set of parameters in pump mode will give the same dimensions as for generating mode, enabling easy analysis of efficiencies in pump- and generating modes for the designs. Changing the sign of the rotation switches between pump mode and generating mode. Fixing the dimensions and changing the head over the unit will give a curve of the efficiencies for operation at these heads. The efficiency curves can then be integrated/averaged to find efficiencies representative of the operation over the duration of the head change, and pump and generating efficiencies can then be combined to find a cycle efficiency. The cycle efficiency is mapped against rotor height and rotational speed and the optimal design is chosen based on the highest efficiency.

For the analysis presented using the analytical model all gap clearances are set to 1 cm independent of rotor dimensions and rotational speeds.

The model has been partially calibrated. 2D CFD results have been investigated for the flow in the rotor-casing gap and the rotor-rotor gap. These 2D results were obtained on a medium scale geometry (rotor diameter of approx. 0,24 m) but the velocity profiles for the gap flows had typical turbulent velocity profiles and using the calibrated model on larger protype scale is therefore considered to be a valid extrapolation with respect to these gap flow physics.

The rotational speeds investigated are all synchronous speeds, thus explaining the non-integer values for this parameter seen in the results.

In section 8, the analysis using the analytical model is extended including fish mortality.

3.1 Verification of the model

A 2.5D (sometimes called a quasi-2D) CFD simulation has been run on a small-scale geometry, with properties shown in Table 1.

Table 1 – Reference properties for analytical model verification with 2.5D CFD

Casing radius	Rotor radius	Rotor height (one mesh cell height)	Rotor-rotor gap (average numerical value)	Rotational speed (rps), turbine mode	Differential pressure
120mm	119,9mm	1,0mm	0,688mm	6,667	10^5 Pa

The analytical model was used and the results showed that the Reynolds number for the rotor-casing gap flow was below 2300, indication laminar flow, whereas the rotor-rotor gap flow had a Reynolds number of slightly more than 40000, in the turbulent regime but a low value for turbulent flows. The correction factors (found in Eq. A7-A12 in Appendix) for the rotor-casing gap flow phenomena were therefore not applied, ultimately resulting in laminar calculations at this location. A one fifth power law velocity profile was used to find correction factors for a less turbulent profile than implied by the one seventh power law, and these factors used for the rotor-rotor gap calculations. (10,98 and 2,75 instead of 13,03 and 3,25 for the velocity gradient correction factors and 0,33 and 1,09 instead of 0,25 and 1,18 for flow correction coefficient for parabolic and linear cases respectively). The leakages and torques linked to the rotor ends were taken out of the equation for the efficiency, effectively turning the analytical model into a 2D model when using a rotor height of 0,01mm.

The CFD results gave an average efficiency of 82,377 % and an average mass flow of 0,25172 kg/s. The analytical model gave an average efficiency 75,63% and an average mass flow of 0,2508 kg/s.

Considering the very small scale of this quasi-2D analysis and the relative importance of the velocity gradients of both torques and flows on the efficiency of the problem the model is considered verified for the effects that occur at rotor casing gap and at rotor-rotor gaps. Verification of the model including the end gap effects will have to be performed using a different set of data, unfortunately not available yet. When the experimental test rig for a model scale PD machine is completed at TU Braunschweig both experimental and CFD results are available for a complete validation of the analytical model. The Chalmers test section was unable to operate in generating mode and will only provide a partial validation of the analytical model. It is therefore favourable to wait for the larger scale TU Braunschweig results for this.

3.2 Generating mode

The efficiency curves found for generating mode are seen in Figure 1.

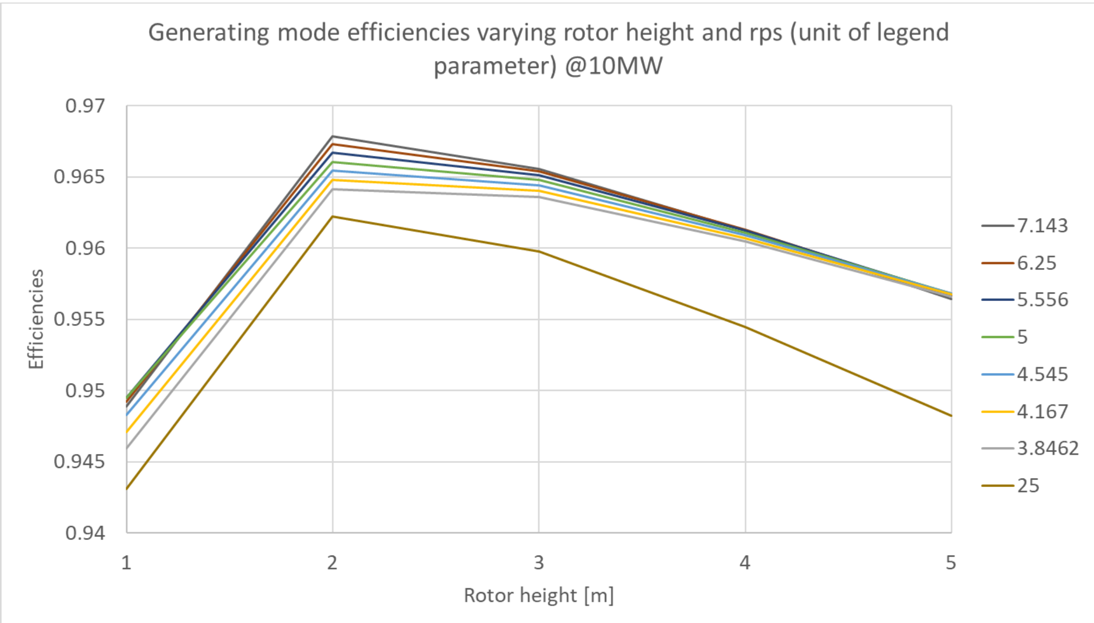

Figure 1: Generating mode efficiencies for different designs changing rotational speed [rps] and rotor height

As expected, the curves are looking like typical efficiency curves, with a lower efficiency at each side of a peak value. Higher rotational speeds give higher efficiencies, and the reader is reminded that these efficiencies are not for different rotational speeds of one fixed design, but for designs using a fixed power. Fixing the rotor height while increasing the rotational speed will lead to a unit with reducing diameter. Fixing the rotational speed and increasing the rotor height does the same. This is what is meant as “design” in this context. Figure 1 is therefore showing the efficiency of 40 different designs; five rotor heights times eight rotational speeds.

The case of rps=25 is included to show that the efficiency predicted by the model drops off at higher rotational speeds, which is not clear based on the curves for lower rotational speeds but is something which is expected by an efficiency model. Curves for higher rotational speeds than rps=7,143 are not shown in Figure 1, but for the analysis of the cycle efficiency higher speeds are investigated.

Investigating the generator mode efficiency for varying heads is one of the steps needed to obtain a full cycle efficiency. The different designs with their respective rotational speed n and rotor height Z subjected to head variations from H=5 m to H= 10 m with one-meter increments gives efficiency curves shown in Figure 2. This analysis is performed for the rotational speeds chosen for the cycle analysis.

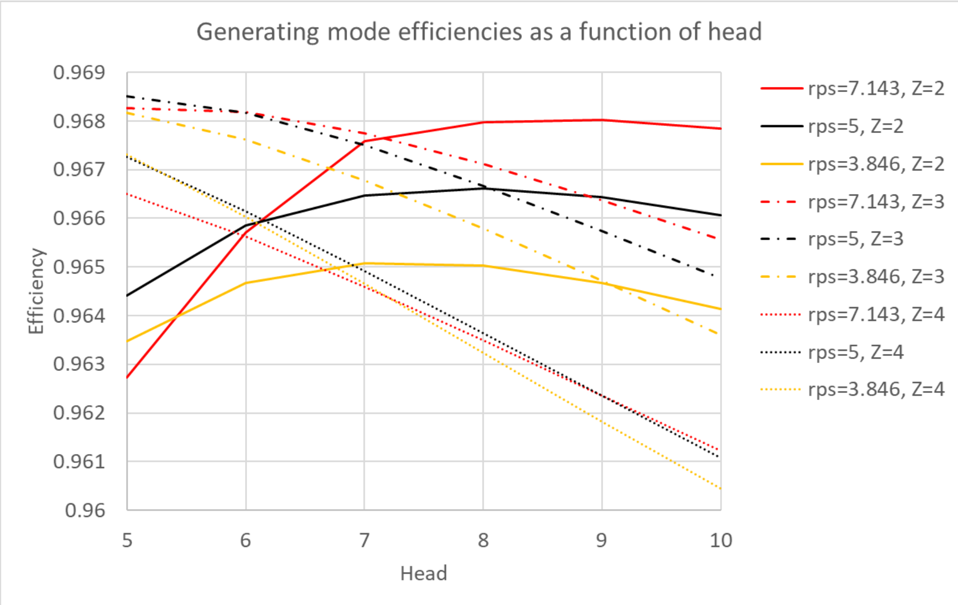

Figure 2: Efficiencies as a function of head in generating mode

Figure 2 shows the efficiency of generating mode subjected to head variations. The trends are quite clear; the higher lobe heights (implying smaller rotor diameter) the efficiency suffers most at higher heads, and the efficiency curves are quite linear. For lower rotor heights the efficiency penalty shifts from high heads to lower heads, as well as the difference in efficiency due to changing rotational speed increases.

3.3 Pumping mode

The efficiency curves found for pumping mode are seen in Figure 3.

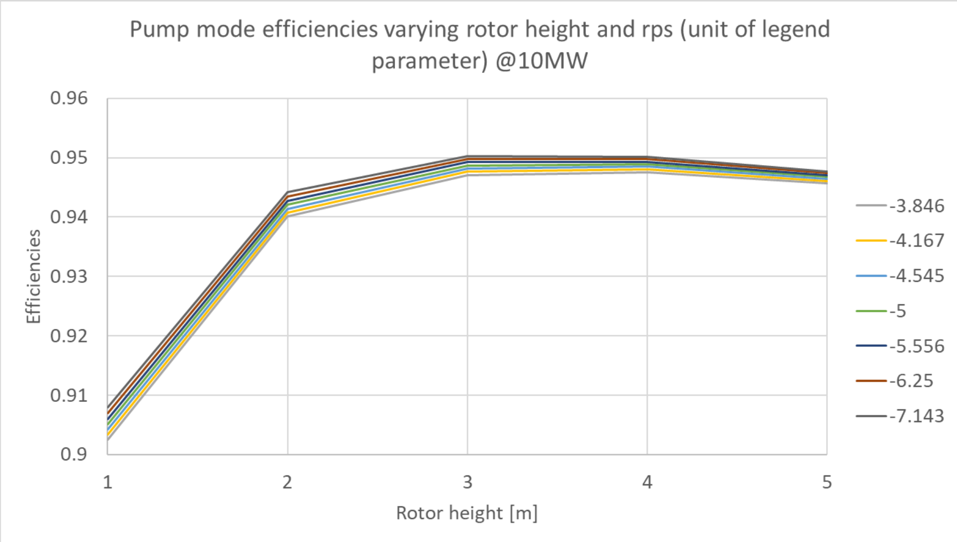

Figure 3: Pump mode efficiencies for same rotor height and rotational speed [rps] (however negative rotation) as the generating mode

The negative value for rps is simply because generating mode rotation is defined as positive and pump mode has the opposite direction of rotation. The efficiency curves for pump mode are also showing the expected characteristics of a peak efficiency, but opposed to generating mode the efficiencies are decreasing for higher rotational speed.

The same (negative) rotational speeds and rotor heights and heads are investigated in pump mode as well. The result is seen in Figure 4.

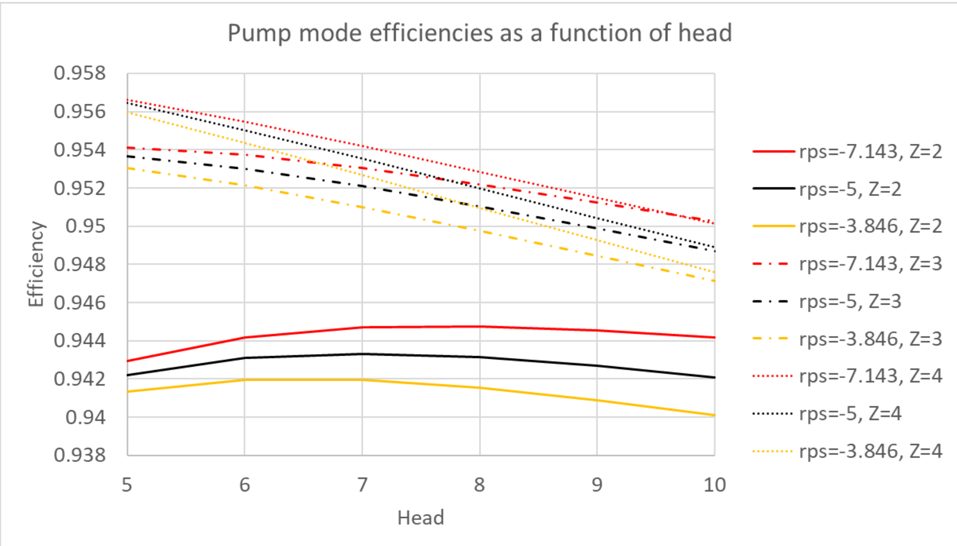

Figure 4: Pumping mode efficiencies corresponding to reversed rotation of the same generation design

The same trends are seen here as for head variations in generating mode; for higher rotor heights the efficiency curves become more linear and decreases with head, and the efficiency suffers more at higher heads. However, the efficiency increases with increasing height, the opposite relation as is seen in generating mode. This indicate that there will be an optimal cycle efficiency for a single design.

3.4 Cycle efficiency

Obtaining a cycle efficiency, one must basically integrate the efficiency over one cycle to obtain the average value. This would include things like the head-flow relation of the reservoirs as well as the characteristics of the unit itself. The characteristics of the units are included in the efficiency curves, but since no reservoir is defined as a base case, we assume that the appropriate average generating efficiency for the 10m-5m head variation (simply chosen for this investigation) will be the average of the values seen in Figure 2. By the same argument we use the average values for pumping efficiencies seen in Figure 4. The total efficiency of a combined pumping-generating cycle will be the generating and pumping average efficiencies multiplied. The result is seen in Figure 5.

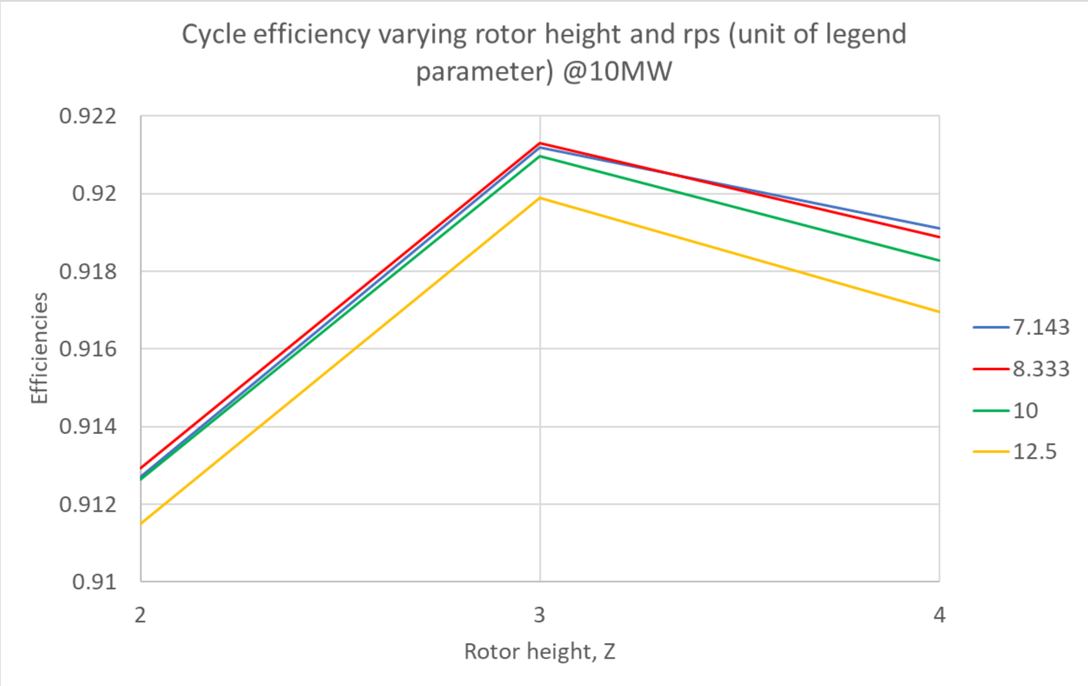

Figure 5: Full cycle efficiencies

The peak cycle efficiency is seen for a rotor height Z=3 m. To be able to easier see at which rotational speed the peak efficiency occurs, the cycle efficiency for Z=3 as a function of rotational speed is plotted in Figure 6.

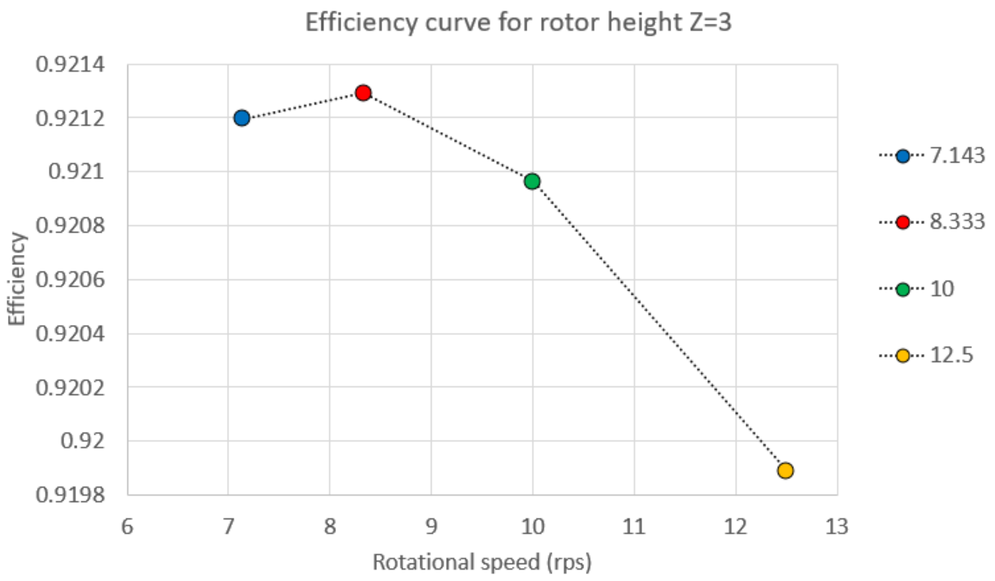

Figure 6: Cycle efficiency for Z=3 at varying rotational speeds

The peak cycle efficiency of the analysis is found at rotational speed rps=8,333.

Throughout this section the rotor height has been changed with increments of one meter, which is quite coarse. However, obtaining the efficiency peak at Z=3 m a refined investigation can be performed around this value with smaller variations in the rotor height. For the scope of this work, it has not been found necessary to do this. Concluding on the section for optimization based on cycle efficiencies for a 10MW unit operating at head levels between H=5 and H=10 meters we find the main parameters to be:

Synchronous speed:	Rotor diameter:	Rotor height:	Cycle efficiency:
500 rpm (8,333 rps)	**2,814m**	**3 m**	**92,13%**

4 Brief overview of experimental setup

This section presents a brief overview of the experiments presented in deliverable D2.5, which were used for validation of the CFD. A tri-lobe machine with straight rotors and cycloidal profile was decided as a reference design. The design of the rig was developed in collaboration between Chalmers and NTNU, and the model scale rig was assembled and prepared by the Chalmers group. The full report on the experimental rig and measurements can be found in deliverable D2.5.

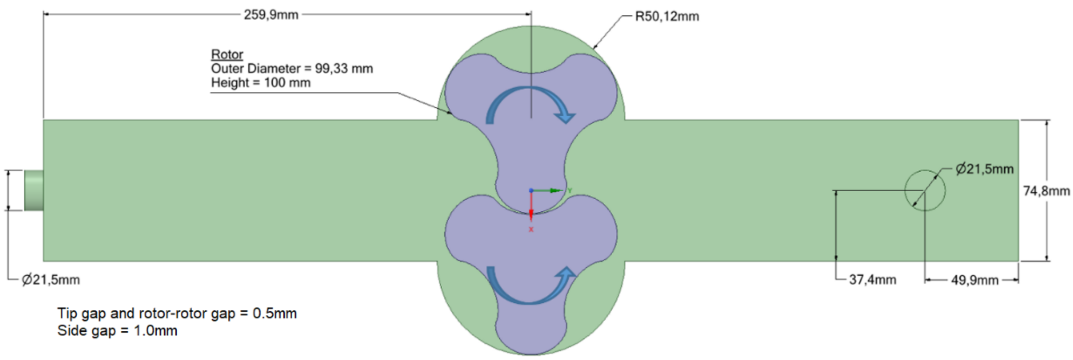

Figure 7 – PD RPT conceptual design

As shown in Figure 7, the experimental rig consisted of two pipes connecting to the main channel which contained the PD RPT. A set of experiments in pump mode was prepared, and later the design was improved by including a diffusor in the inlet, so the transition was smoother.

Figure 8 shows the final CAD geometry and Figure 9 shows the comparison between the pump characteristic curves in the design with and without diffusors.

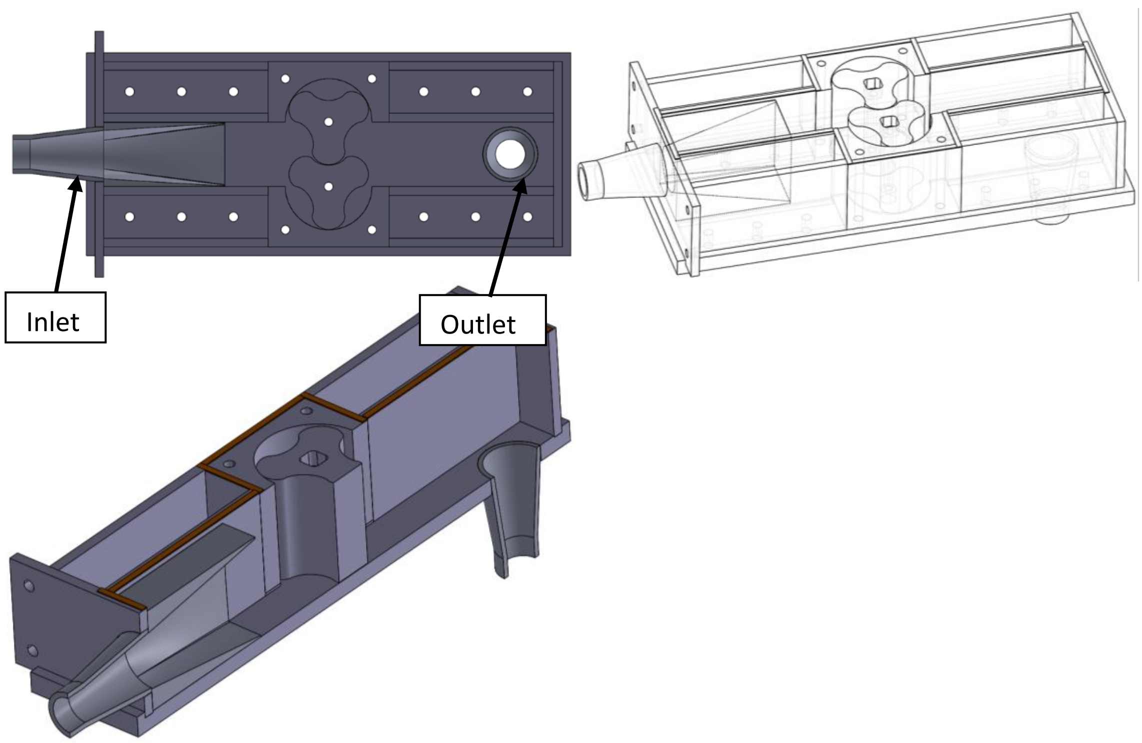

Figure 8 – Final CAD geometry.

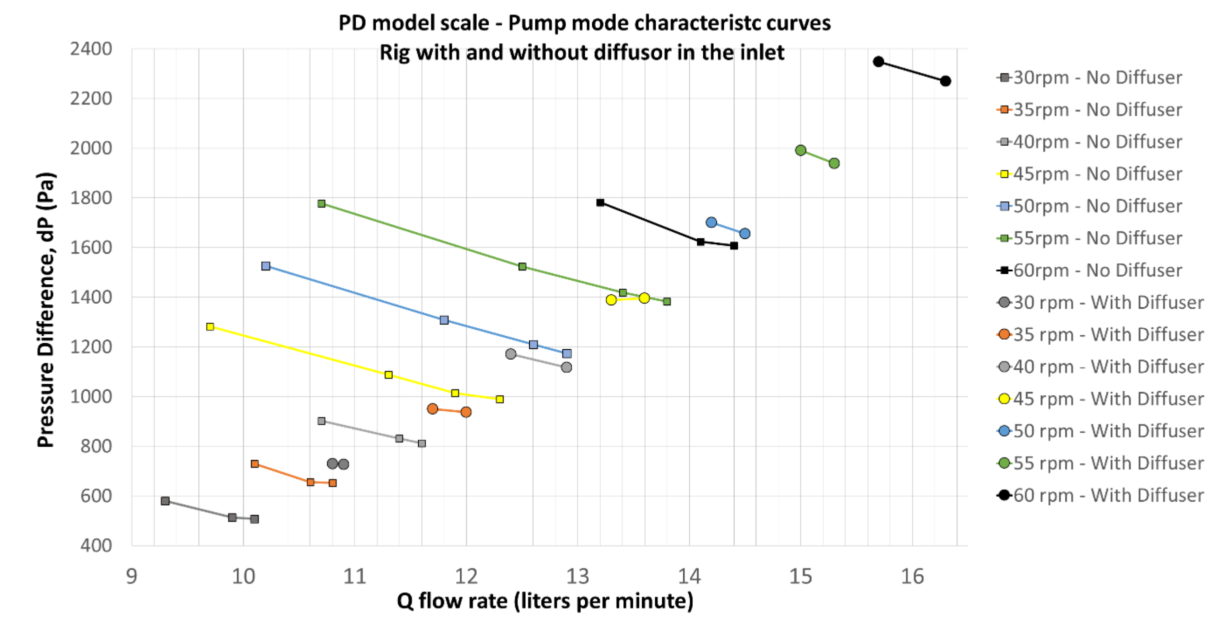

Figure 9 – Pump characteristic curves: with and without diffusor

In Figure 9, the characteristic curves for both geometries present a linear relation between flow rate and pressure difference, where the slope of the curve represents the leakages that occurs through the gaps, which is also known as "slip". We can also notice that, for the same rotation speed, the curves between geometries differ considerably, even though the only additional features, the diffusers, were included in the inlet and outlet and did not interfere directly in the rotors zone. Thus, the diffusors were able to reduce drag and increase the flow rate. The small scale of the experimental model is very sensitive to variations in geometry or operation conditions, even small ones like the change in the gap sizes due to assembly and manufacturing reasons. Kang et al. (2012) addressed the same difficulties in measurements and measuring equipment can have significant errors.

5 Numerical simulation – CFD Validation

The PD RPT was simulated and optimized via computational fluid dynamics (CFD) through the software ANSYS CFX. The simulations were prepared with single-phase water, transient setup, k-ω SST turbulence model and isothermal conditions. Simulations and boundary conditions were defined by the rotor rotation speed, static pressures at inlet and outlet (modelled as "opening" in CFX), representing the pressure difference or water head. No-slip walls were used to treat all the surfaces in the model.

The first batch of simulations used the Immersed Boundary Method (IBM) to interpolate values along the solid-fluid interface at the rotor surface while introducing a penalty source term when fluid tries to occupy the solid domain. This method promised to gain computational time since the solver does not need to recalculate the numerical mesh for each time step. Although, after many iterations with this method, the IBM proved to be numerically unstable and did not guarantee that no flow went through the rotors, and the leakages were under- or overestimated.

In order to apply a more stable numerical method and to retrieve better values of leakage, a new software was introduced. TwinMesh is a specialized software for positive displacements machines, it can create high-quality numerical mesh for every angle of rotation of the rotors, and it also prepares and export the basic setup for ANSYS CFX. Additionally, investigation regarding the sensitivity of parameters such as the designed gaps are more easily implemented.

New simulations were prepared to investigate and compare results for three operating conditions in the design with diffusor. These operating points are shown in Table 2 and follow the same conditions described in deliverable D2.5 that produced PIV results for supporting the validation of the CFD results.

Table 2 – Global parameters for investigated cases

Mode	RPM	Flow, LPM	dP tot, Pa
Pump	55	13	1230
Pump	45	11	1058
Turbine	45	29.3	-858

The mesh was generated separately for the stationary and rotating parts, and they consist of 2.2M and 3.5M cells respectively. The mesh quality for the rotating components was ensured and verified via the TwinMesh software, and the full simulation had Courant number and Y+ as physical and numerical quality indicators. Figure 10 below presents the meshes used for the numerical validation.

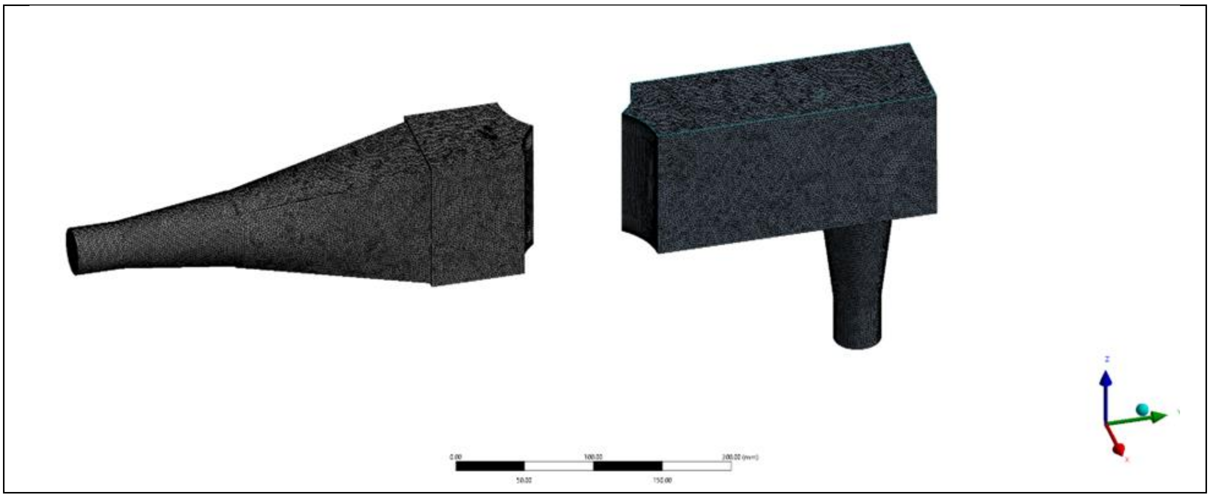

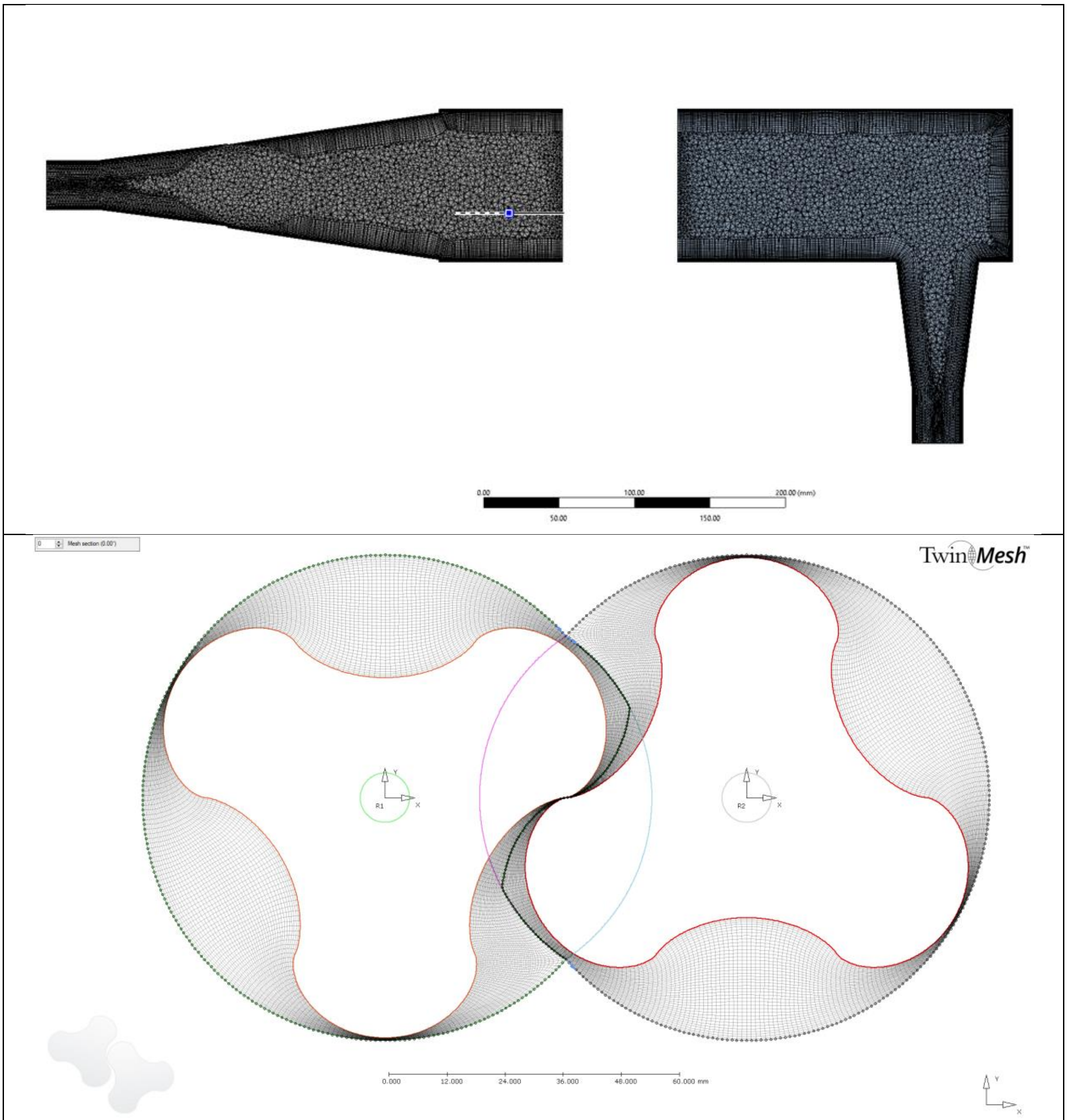

Figure 10 – Mesh of the stator and rotating components created, respectively, in ANSYS and TwinMeshTM.

The CFD results showed convergence on average values even before the rotor makes a full turn. However, flow structures at the same rotation position might present some variations between different water strokes. Figure 11 shows flow rate and torque calculations for Chalmers experimental design in pump mode and 55 rpm, and it numerical stabilizes little after 50 time steps (corresponding to 50º of rotation in this simulation), and the characteristic periodic pulsation behaviour which is presented for three-lobe machines.

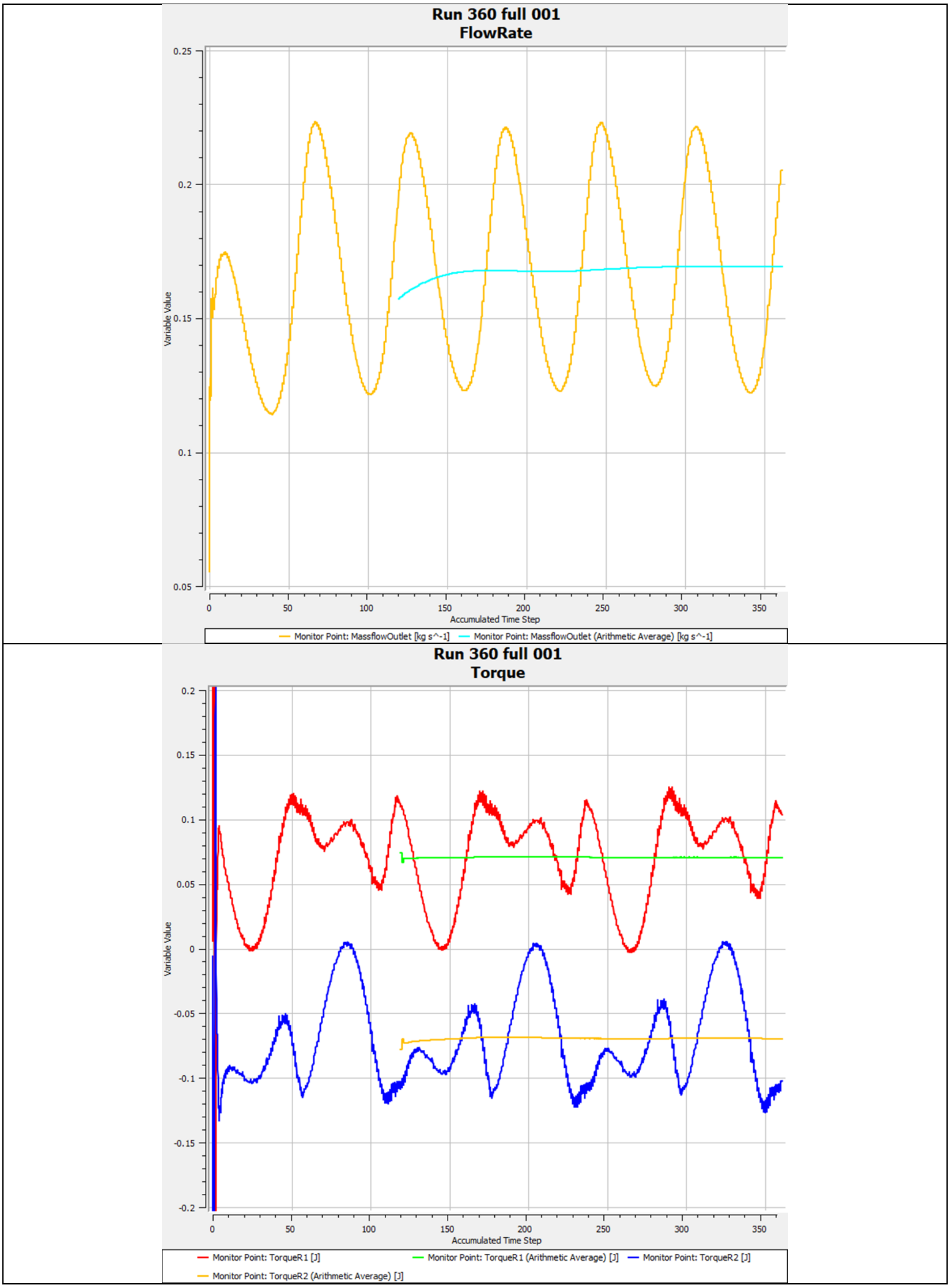

Figure 11 - Pulsation characteristic curves for lobe machine in pump mode at 55 rpm and respectively average values. Top: Flow rate. Bottom: Torques for rotor 1 and rotor 2.

Table 3 shows the average flow rate values for the three studied cases.

Table 3 : CFD Validation, Experiments and CFD comparison				
Mode	**RPM**	**Flow Rate Experiments, LPM**	**Flow Rate CFD, LPM**	**Error**
Pump	55	13	10.13	-22.1%
Pump	45	11	6.12	-44.4%
Turbine	45	29.3	41.66	+42.2%

As shown in Table 3, the CFD results produced different flow rate values compared to the experimental data. As explained before, flow rate and other values are very sensitive to the smallest variations in gap sizes, and therefore a sensitivity analysis was undertaken. Because of assembling reasons, the side gaps (gap between rotors' axial surface and casing) seemed to be the parameter that could have real value significantly different than the aimed 1mm in the design project.

Another model with 0.5mm of side gaps was created for the pump mode case at 55 rpm. This time, the CFD results produced a flow rate of 18,8 litres per minute, which is around 45% bigger than the experimental value. With the help of the analytical approach described in the Appendix, we could estimate the real side gap size of 0.85mm by applying a linear interpolation for the adjusted flow rate, which is the expected flow rate provided by the analytical equations after it has been adjusted by the relative error with the flow rate provided by the CFD simulations. Table 4 below shows the sensitivity analysis using the analytical approach for pump mode at 55 rpm.

Table 4 : Sensitivity analysis for pump mode case at 55 rpm.

Side gap (mm)	Adjusted flow rate, analytical approach (LPM)	Error with experiment
1.0	10.07	-22.51%
0.9	12.18	-6.27%
0.8	14.21	9.28%
0.7	16.07	23.62%
0.6	17.72	36.28%
0.5	19.11	46.96%

Similar sensitivity analyses were created for pump and turbine modes at 45 rpm in order to check if the side gap change in pump mode at 55 rpm had similar results. When adjusted by analytical equations, for pump mode at 45 rpm, we found an estimated side gap of 0.92mm. For turbine mode at 45 rpm, the estimated side gap was around 0.78 mm. The small differences between different cases confirm the high order of sensitivity when gaps change just a bit. Although small, the differences between estimations for the real side gap might suggest that small variations in other gaps (such as rotor-rotor gap) could push all three cases to the real value for the side gap size.

Two CFD simulations executed with the same operating conditions but implementing two different side gap values present different localized leakages near the side gaps. However, since the projection of the geometries are exactly the same at the plane that crosses in the middle of the height of the rotors, the flow pattern and velocity profiles should be very close to each other when it is near to the rotating parts. The different levels of leakages produced in the side gaps should only disturb and produce different flow velocity ranges when those volumes are already relatively far from the rotors. For that reason, comparisons between PIV data and CFD should be adequate when close to the mid-plane and to the rotors. In other words, different leakage levels produced in CFD should soften or increase the contrast between PIV and CFD images when they are no longer close to the rotating parts.

Figures 12 to 17 below show the comparison between PIV and CFD results, thus structures in flow can be compared and analysed. As described in D2.5, the PIV results are phase-averaged, and the small thickness of the laser sheet introduces some averaging along that thickness. The CFD results are presented for a single time step, at a single position along the z-axis. It is assumed that the RANS turbulence model gives a flow that is periodic in time. The same rotor phase angles as described in D2.5 are used, denoted “0”, “15” and “30”.

Colour schemes in the following images are slightly different. The images are made using different software, so it turned out to be very difficult to make these identical in due time.

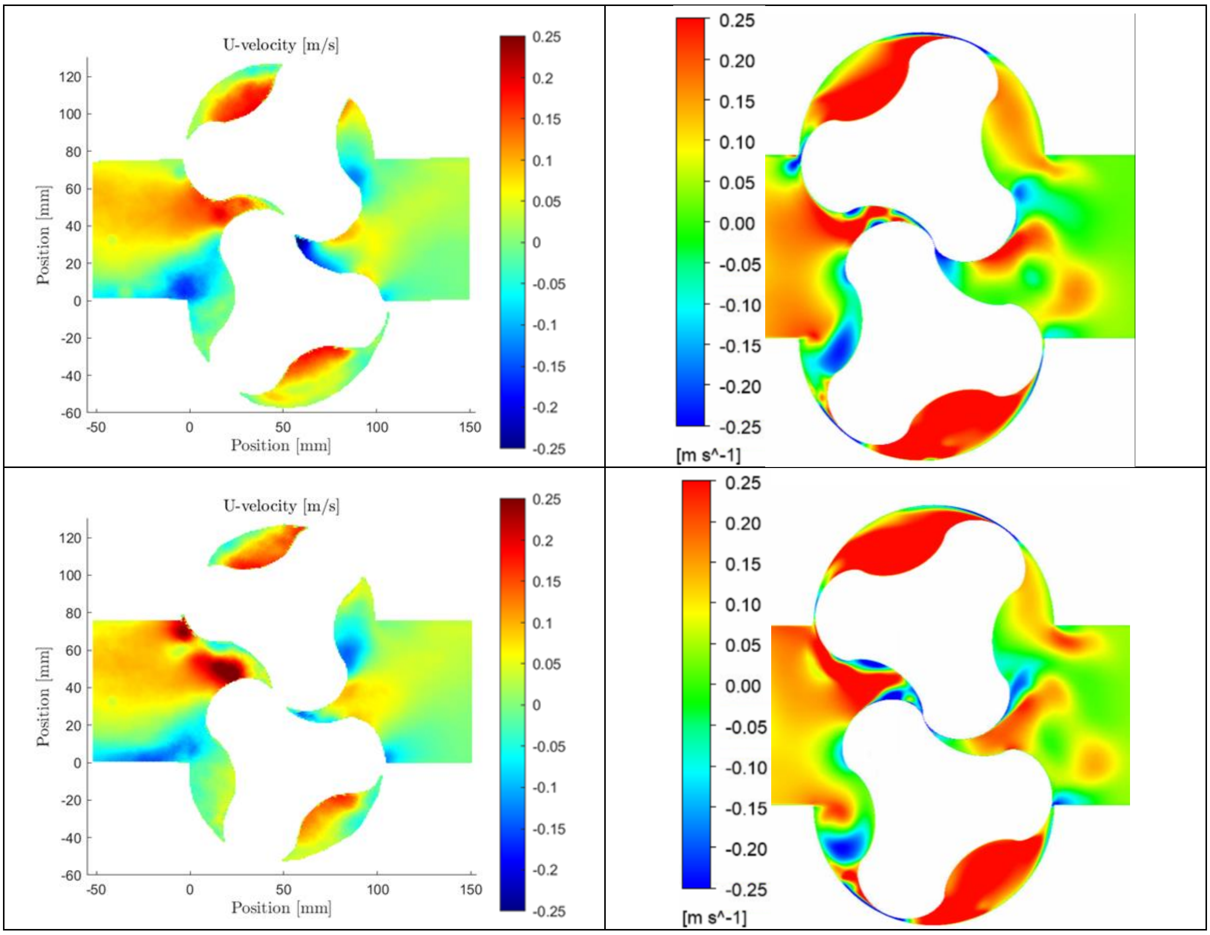

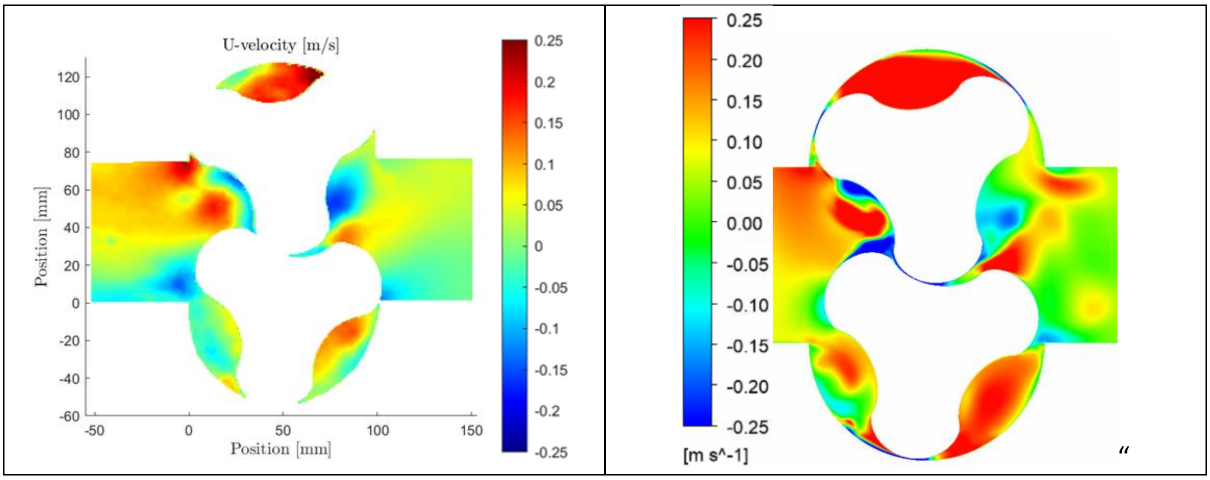

Figure 12 - Pump mode at 55 rpm. U-Velocity for positions "0", "15" and "30" degrees of rotation. Left: PIV. Right: CFD.

Figure 12 shows the x-component of the velocity for the pump mode at 55 rpm. In the inlet (left side), we can see higher values in the upper part of both PIV and CFD images as a result of the low-pressure zone created by the rotors when the lobes move apart from each other, which sucks the flow towards the rotor chambers (red zone occupying most of the upper rotor chamber area). In the upper rotor outlet, we can see the water to continue being pushed out of the chambers, despite the difference in color scheme, but still positive values. Also, in both PIV and CFD upper rotor, we can spot a blue area slightly above the lower lobe. That blue color correctly indicates that the lobe surface is moving towards the inlet, thus showing negative values for velocity. The outlet shows a big portion of green, near zero velocities, and some smaller areas in yellow and red for all rotor positions, which indicates that the fluid is being pushed upstream. Between the rotors, around the rotor-rotor gap, we see a blue area that represents the backward leakage through that gap in both PIV and CFD, that is from the high-pressure side (outlet) to the lower pressure side (inlet). Leakages in the tip gaps, which is only seen in the CFD results due to the resolution level, also depicts the leakage from outlet to inlet direction. Finally, in the inlet side of the bottom rotor, the PIV indicates a bigger still or backflow area before the water gets trapped by the lower chamber. On the other hand, CFD predicts a much smaller area of backflow, much closer to the bottom rotor surface, while the main stream is still positive and advances towards the rotor chamber. However, we can see from the "30" degree CFD image that a bigger green area starts to form when the lobe gets closer to the sharp edge. And if we observe the upper rotor in the "0" position, a soft blue point indicates the backflow in that mirrored position, which indicates the vestige of the backflow before the water gets completed involved by the rotor chambers. Finally, the velocities inside the closed chamber in the lower rotor follow the same pattern in both PIV and CFD, where a big portion of red indicates the flow continues to be pushed towards the outlet.

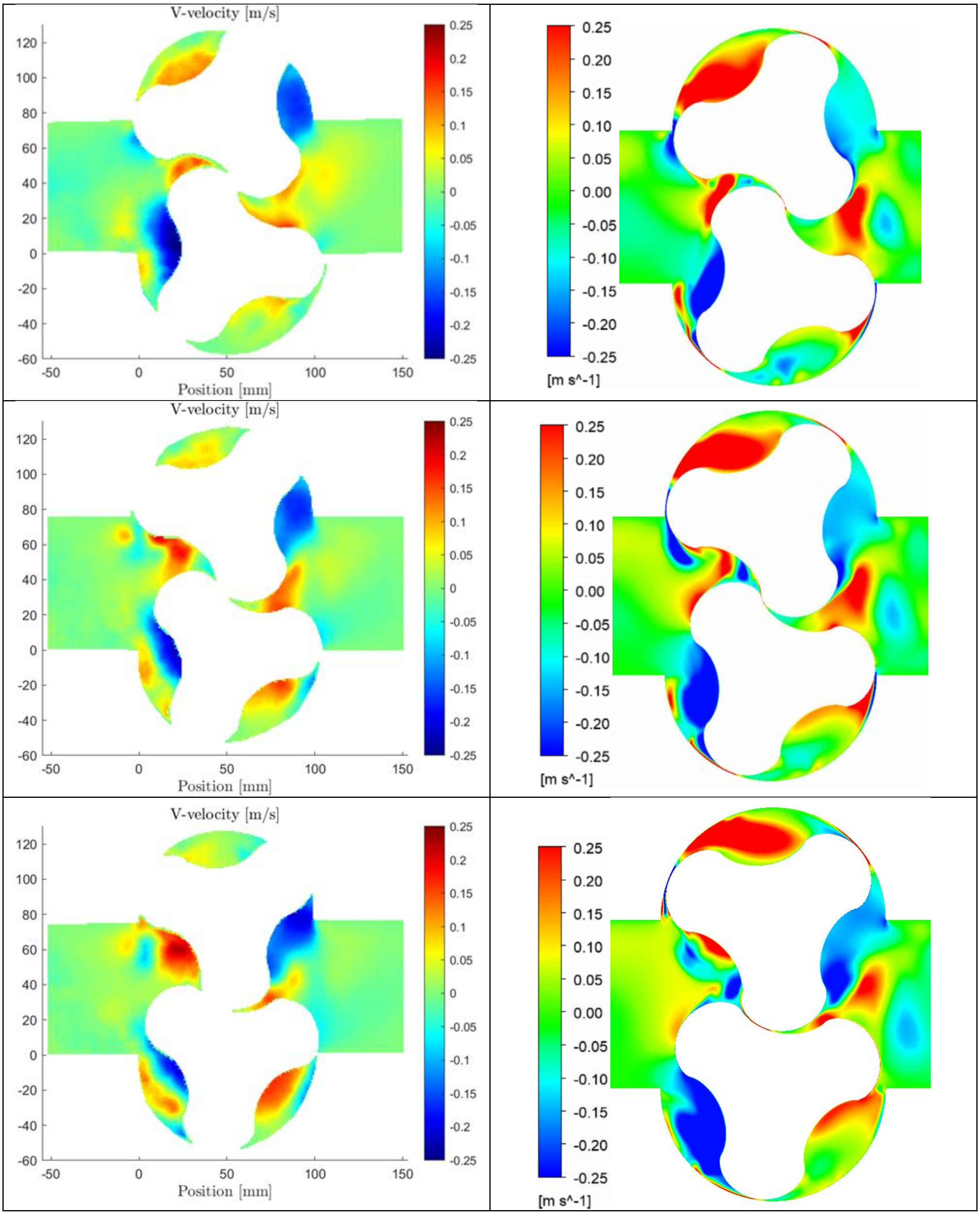

Figure 13 - Pump mode at 55 rpm. V-Velocity for positions "0", "15" and "30" degrees of rotation. Left: PIV. Right: CFD.

Figure 13 complements Figure 12, as it shows the velocity component in the y-direction for the same pump mode case at 55 rpm. Far from the rotating parts, most of the areas are green in both PIV and CFD, corresponding to near zero velocities in the y-direction. Red and blue areas are all well represented, following the rotor rotation direction for each zone of interest, where the water is being pushed up or down by the rotor's movement. Colours inside the gaps follow the same logic explained in Figure 12, with all leakages going from high-pressure side (outlet) towards the low-pressure side (inlet).

Figure 14 and Figure 15 present the same patterns as Figure 12 and Figure 13 since they all represent pump mode. Since they come from different rotation speed scenarios, just the velocity magnitudes are adjusted.

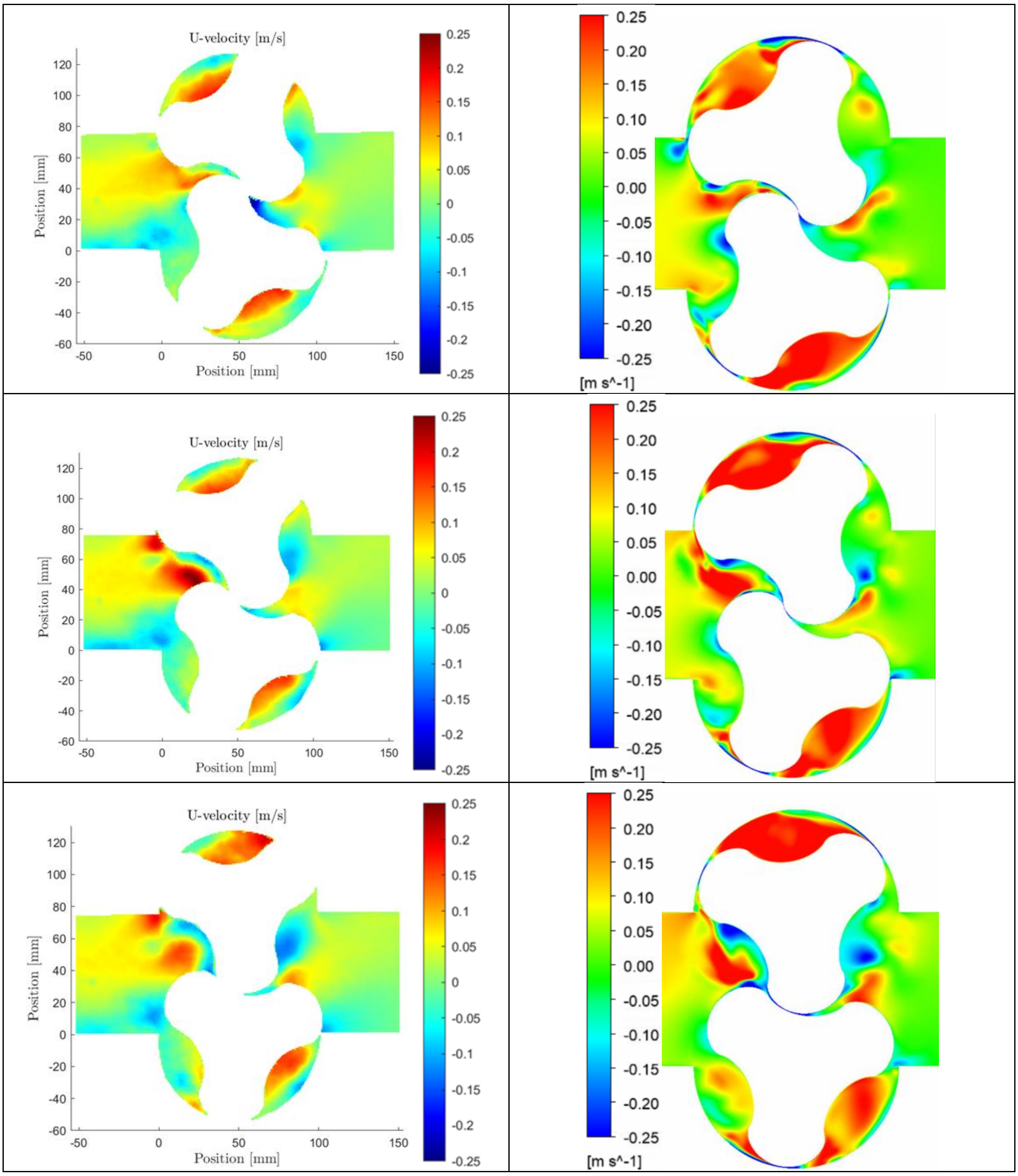

Figure 14 - Pump mode at 45 rpm. U-Velocity for positions “0”, “15” and “30” degrees of rotation. Left: PIV. Right: CFD.

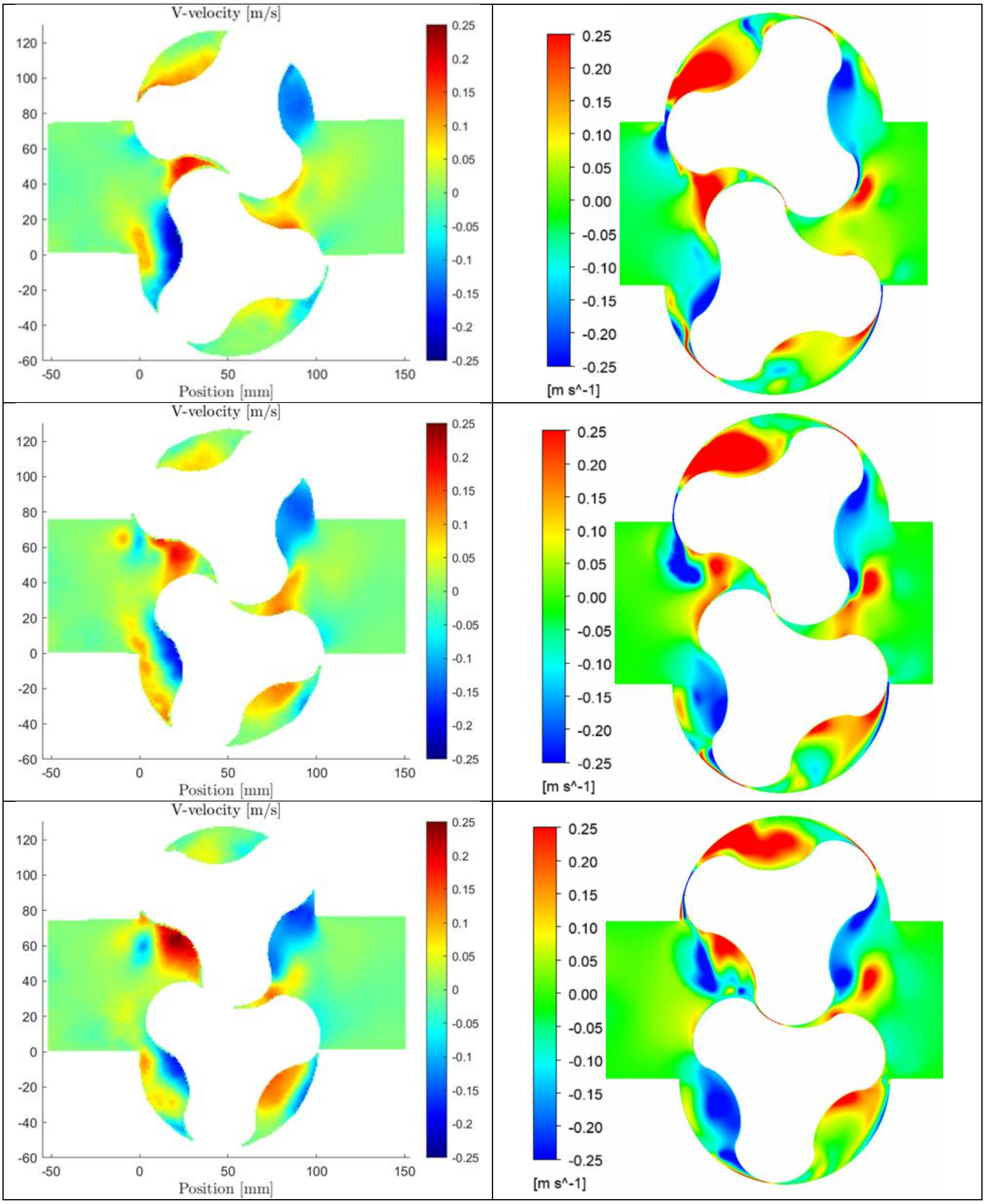

Figure 15 - Pump mode at 45 rpm. V-Velocity for positions "0", "15" and "30" degrees of rotation. Left: PIV. Right: CFD.

Figure 16 and Figure 17 show the x- and y-components of the velocity for turbine mode at 45 rpm. Interestingly, since the experimental setup used the same reference for flow direction, from left to right, much of the flow patterns follow the same behaviour as of the other two pump modes in the previous pictures. Important reminder is to consider each picture inside its own colour scheme.

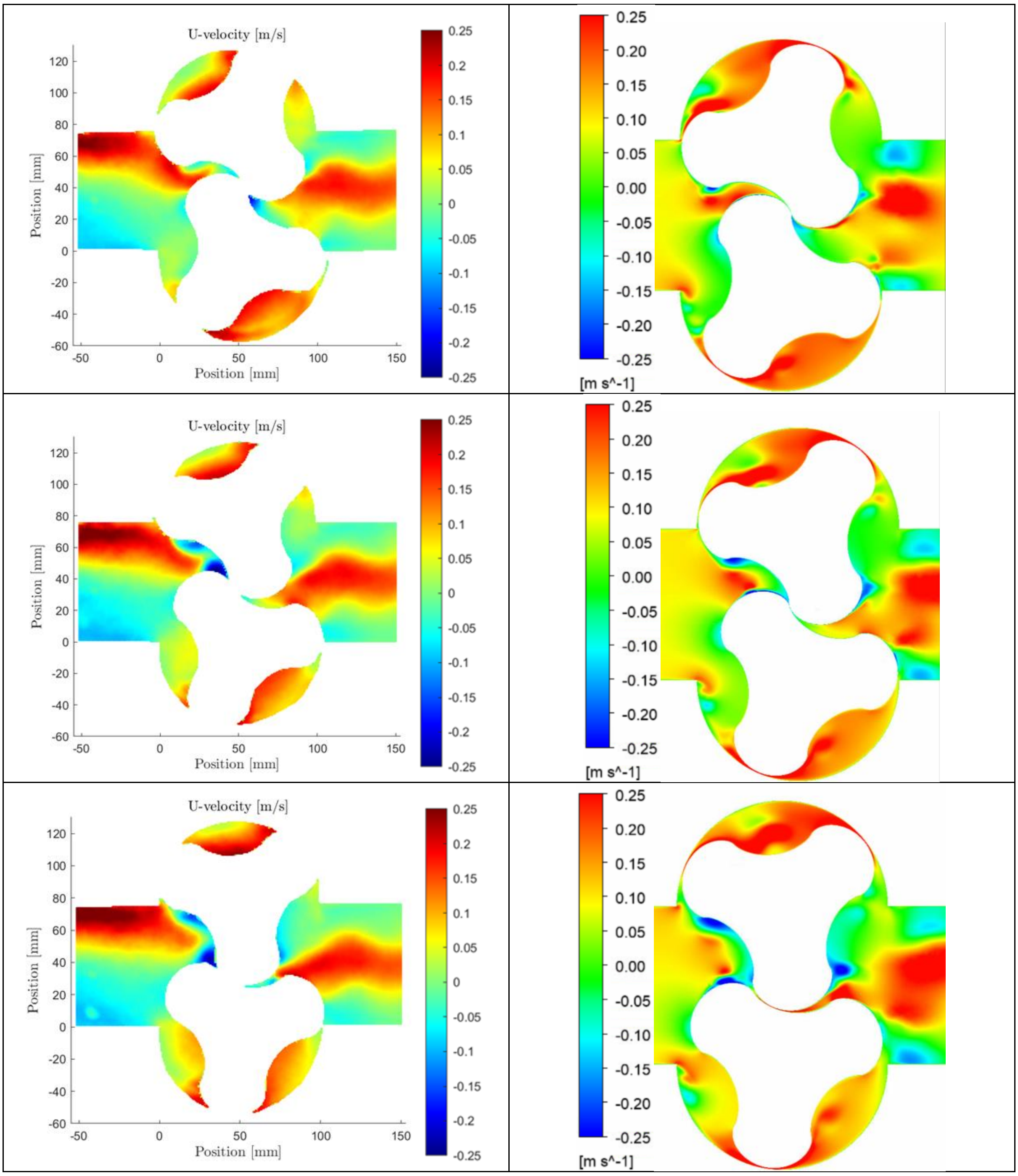

Figure 16 - Turbine mode at 45 rpm. U-Velocity for positions “0”, “15” and “30” degrees of rotation. Left: PIV. Right: CFD.

One important difference between turbine mode and pump mode is that the pressure difference has opposite signs. So, in turbine mode, the leakage happens towards downstream instead of upstream, and we can spot the flow passing through the gaps from the left (inlet) to the right (outlet) side of the pictures. A new flow pattern in turbine mode is the jet that is formed in the middle of the images, right after the rotors in the outlet side. Despite the difference in colour schemes, both CFD and PIV show the same red area surrounded by a thin yellow layer. The CFD shows a bigger area though, which might soften if multiple complete turns are taken into consideration, but that would increase the computational time too much. LES turbulence models could also bring a more detailed flow in the

CFD, but RANS turbulence models provide faster numerical solutions, which is desired for design optimization studies.

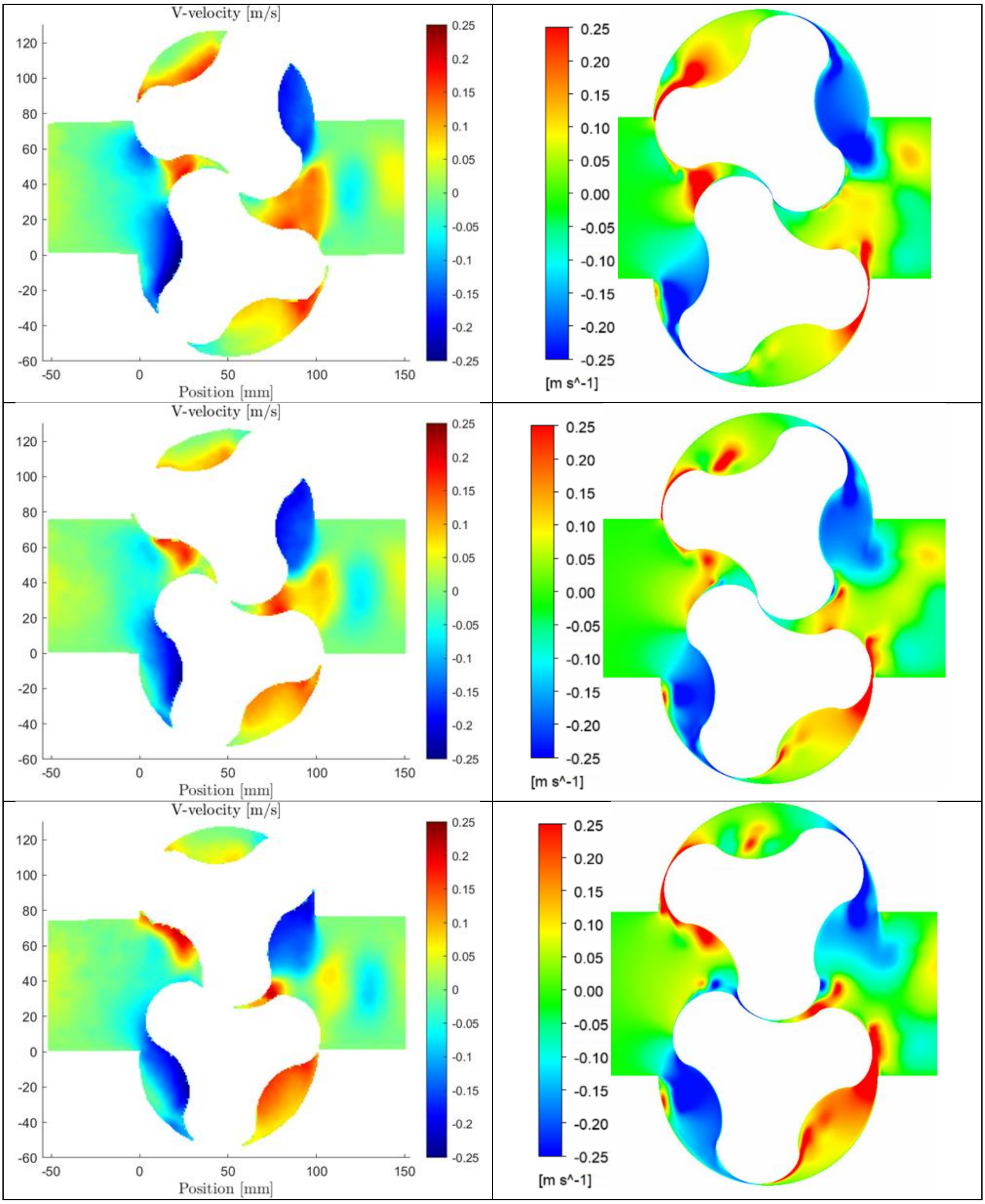

Figure 17 - Turbine mode at 45 rpm. V-Velocity for positions “0”, “15” and “30” degrees of rotation. Left: PIV. Right: CFD.

Finally, Figure 17 shows the same behaviour as for the other V-velocity fields, where red and blue areas also represent the direction of each rotor rotation.

After the sensitivity study for average flow rate, the CFD simulations with side gaps of 1mm showed very similar velocity distributions compared to the PIV data, thus demonstrating that small differences in side gap size did not significantly disturb the flow patterns in the mid plane. In conclusion, the numerical model can be considered validated, and the design optimization can be continued accordingly.

6 Design optimization

Different parameters can be addressed in the PD RPT design to increase efficiency. Some of those have already been thoroughly investigated in the literature, which is taken advantage of here to save resources and not repeat what has already been done. Additional parametric studies have been performed in the present work to complement the conclusions found in literature.

Among the parameters, we studied how clearances affect the efficiency, which rotor surface profile provides the best outcomes (cycloidal or circular shape), how many lobes should the rotor have, the possibility of twisting rotors in the z-direction, different inlet and outlet channel shape (circular pipes or rectangular channel), and other disruptive modifications in the geometry. The rotation speed versus efficiency curve is also presented for the PD RPT design to be studied experimentally at TU Braunschweig as part of the ALPHEUS project.

6.1 Rotor profile

The most obvious aspect to be optimized is the rotor profile, which can affect performance considerably. Two profiles were compared: the circular and cycloidal profile (common choices by manufacturers because the rotor-rotor gaps are constant). Kang et al. (2012) investigated this topic and they found that less pressure drop was generated by the cycloidal lobe. They also stated that the combination of less vortex formation and lower speed helps epicycloidal lobe pump to take an advantage over circular lobe pump, since it would prevent backward flow from the discharge area to suction area. Another advantage for the cycloidal profile was that it generated a characteristic curve with higher slope ratio, which results in higher efficiency of the pump because of the smaller leakage level in pump mode. Plus, the average value of pressure head of epicycloidal lobes was nearly 10% higher than that of circular pump in all studied cases. Finally, multi-lobe pumps with up to 4 lobes were compared, and they found that both tri- and four-lobe pumps provided more stable output and higher capacity than the two-lobe design, with no important differences between the tri- and four-lobe pumps. At the same time, multi-lobes do not improve performance of the pump with respect to efficiency. Therefore, rotors with three lobes with a cycloidal rotor profile were chosen as the design option for the ALPHEUS project and further optimization studies.

6.2 Inlet and outlet channel shapes and sizes

Sonawat et al. (2021) studied the influence of different cross-sectional shaped inlet and outlet pipes in a four-lobe turbine with twisted rotors. They compared pipes with circular, square and rectangular shapes in CFD simulations in order to find the best efficiency shape. The authors realized that the circular shaped pipes resulted in the generation of stronger vortices than for the rectangular pipe, and that recirculation in the flow was also greater for the circular shape. Because of the better alignment of the flow in regard to the rotor area, a rectangular shaped pipe provided higher efficiencies since it reduced the presence of recirculation regions, achieving a 0.824% higher hydraulic efficiency compared to the circular shaped pipe in their study case and design. Figure 18 depicts the design study. A benefit with an optimal shape that is rectangular is that 2D CFD analysis is a good approximation for further analysis, which simplifies further parametric studies.

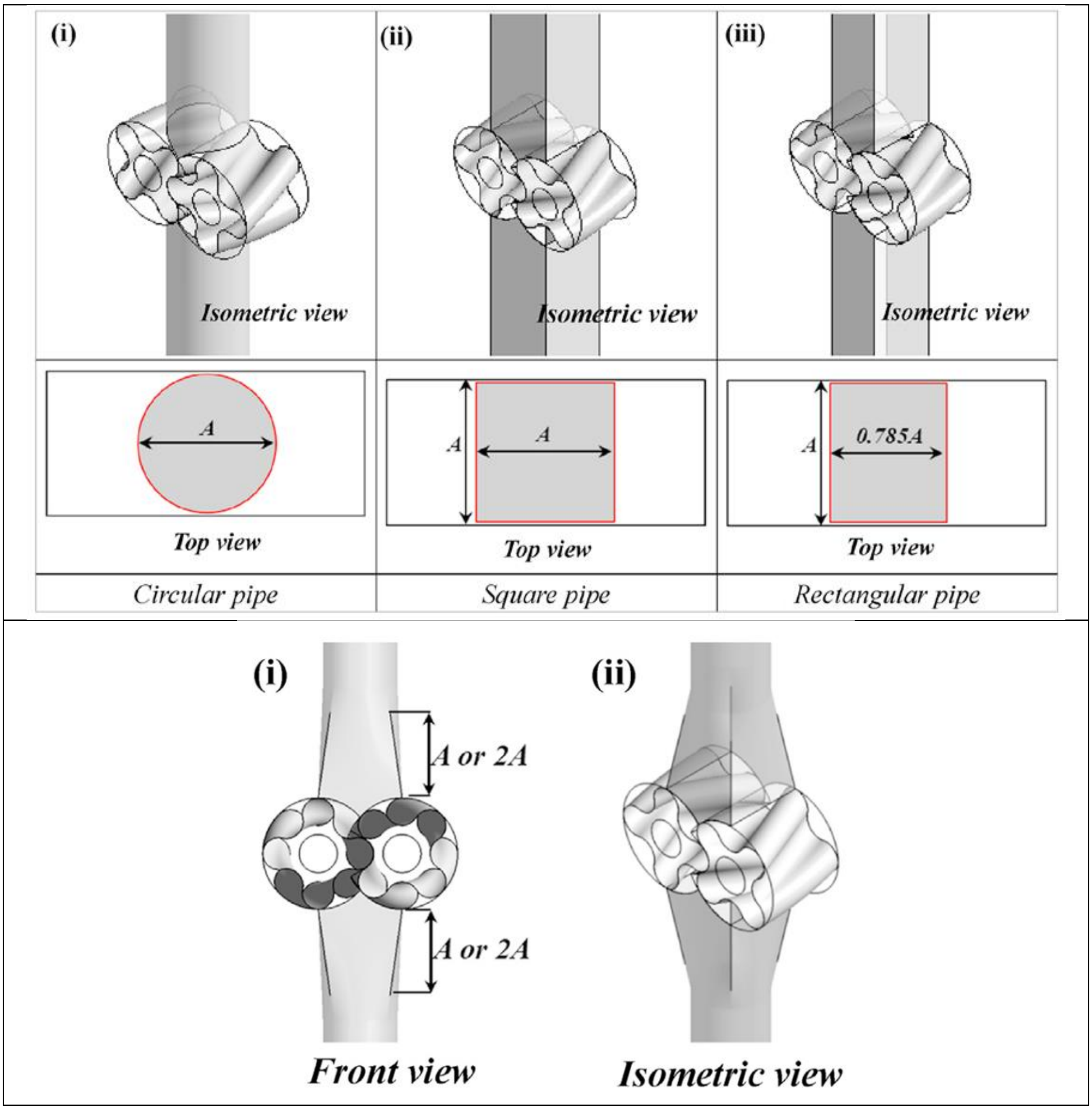

Figure 18 – Top: Cross sectional profiles study for pipes connecting to lobe machine. Bottom: Minimum distance for cross sectional transition. Source: Sonawat et al. (2021).

One question that has not been addressed in previously published work remains: Is there an optimal inlet and outlet pipe width, compared to the rotor diameter? In ALPHEUS we therefore studied the efficiency as a function of the ratio between the pipe width and the rotor diameter (see Figure 19), for a fixed head and rotation speed of the rotors. Figure 20 shows the resulting efficiency curve of this optimization study with 2D simulations. It can be seen that the best efficiency is obtained when the ratio between the inlet width and the rotor diameter is equal to 1. It can also be seen that the sensitivity of the efficiency to the ratio between the inlet width and the rotor diameter is lower at lower ratios and higher at higher ratios.

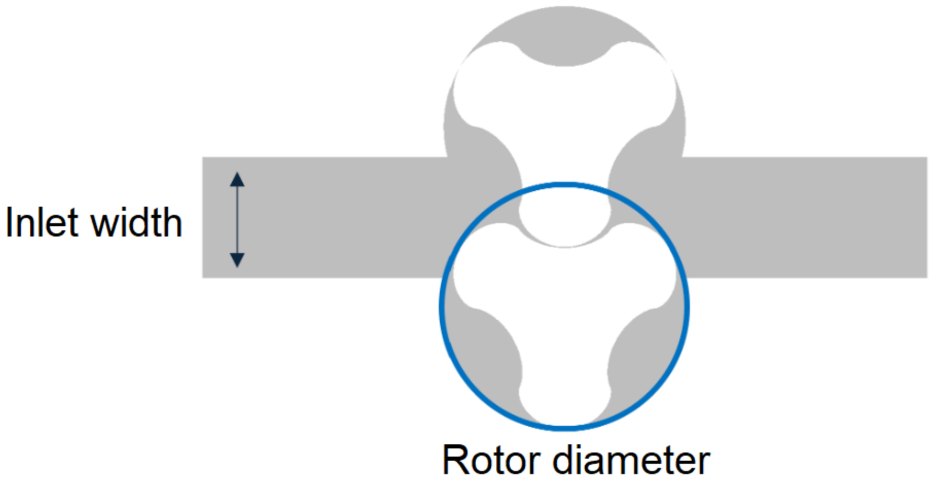

Figure 19 – Inlet width – rotor diameter ratio scheme.

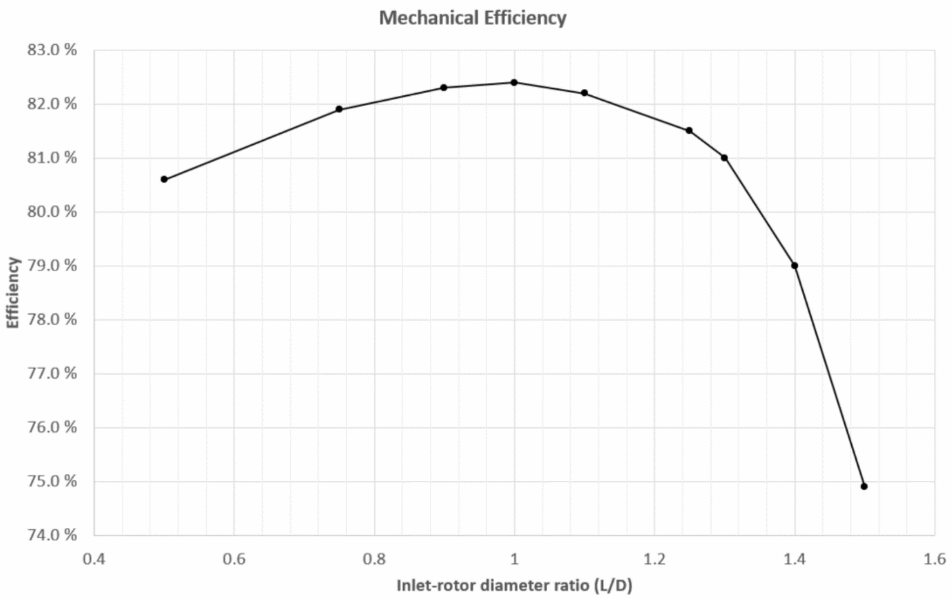

Figure 20 – Efficiency vs. ratio between inlet width and rotor diameter.

In the experimental investigations of the ALPHEUS project a transition from circular to rectangular pipe cross-sectional shape needs to be designed in order to guarantee higher efficiencies. It is also important that the area of the rectangular matches the circular pipe, so the flow rate in the section is still the same, and no losses from increased pressure drop are generated. This has been done in the final design for the measurements to be performed at TU Braunschweig.

6.3 Clearances size

Rotary lobe pumps and turbines present clearances between rotors and casing, and also clearances between both rotors. These gaps are expected to prevent the rotors from touching each other or to touch the casing at any instant of the pump or turbine operation. If there is any contact point, the machine operation may be influenced, but most importantly it may cause excessive wear or even sudden total breakdown. Plus, depending on the clearance sizes, cavitation and unwanted vibrations can come to place. Thus, we need to determine how big or small those clearances should be to guarantee the highest efficiency while mitigating the operation problems listed before.

Phommacchanh et. al. (2006) covered many common aspects to the ALPHEUS PD RPT machine. They also studied a three-lobe turbine, but their rotors were designed to have a spur gear around the curve shape in order to improve the torque transmission between the two rotors. Their main interest was to determine the efficiency of the PD turbine and the influence of the leakage on efficiency. They showed that their PD turbine was much more efficient than a conventional turbine and that it can sustain high efficiency under a wide range of operating conditions. They also found out that the efficiency of turbine mode is much improved when reducing the clearance between the rotating and stationary parts of the turbine because of the amount of water leakage through those gaps. That same conclusion also has background in the fluid mechanics Couette flow, where the velocity is proportional to the gap size squared, where the bigger the gap, the higher the speed, and therefore the higher the leakage. Complementary to that conclusion, they noticed that the torque efficiency η_T[1] of small side clearances decreased noticeably at low differential pressures. But the improvement of the volumetric efficiency η_v[2] of the turbine with small side clearances was much higher than the torque efficiency reduction. Also, the PD turbine with a smaller side clearance obtained much higher output power and consequently higher efficiency than the case with a large clearance at the same head and flow rate.

Kang et al. (2012) also found the same conclusions, and proved that smaller clearances between rotor and casing walls produced much higher efficiencies.

In conclusion, for the optimal design of the reversible lobe pump turbine, tip gaps and side gaps should be as small as possible, and manufacturing and assembling limits will define their final size. Only the rotor-rotor gap needs to be further investigated and tested on the best size possible.

In regards to the rotor-rotor gap (g_{rr}) influence over the efficiency, different scenarios can be raised. Combined with the water head, different rotation speeds might lead to different optimized rotor-rotor gap because it will produce different magnitudes of low- and high-pressure zones around the rotor-rotor gap. Therefore, at least two simulations should be investigated to check for an optimized rotor-rotor gap, one simulation at a high rotation speed and another at a low rotation speed.

For high rotation speed, a 2D simulation was prepared for pump and turbine modes with fixed water head of 10m, rotor with cycloidal profile and outer diameter of 240mm and tip gaps of 0.1mm. The results are presented in Figure 21. It can be seen that the efficiency increases with a reduced rotor-rotor gap in both pump and turbine mode, and the effect is highest in pump mode.

---

[1] η_T=actual torque on shaft/ideal torque from the flow

[2] η_V=displaced volum pr time by the lobes/flow through the unit (including leakages)

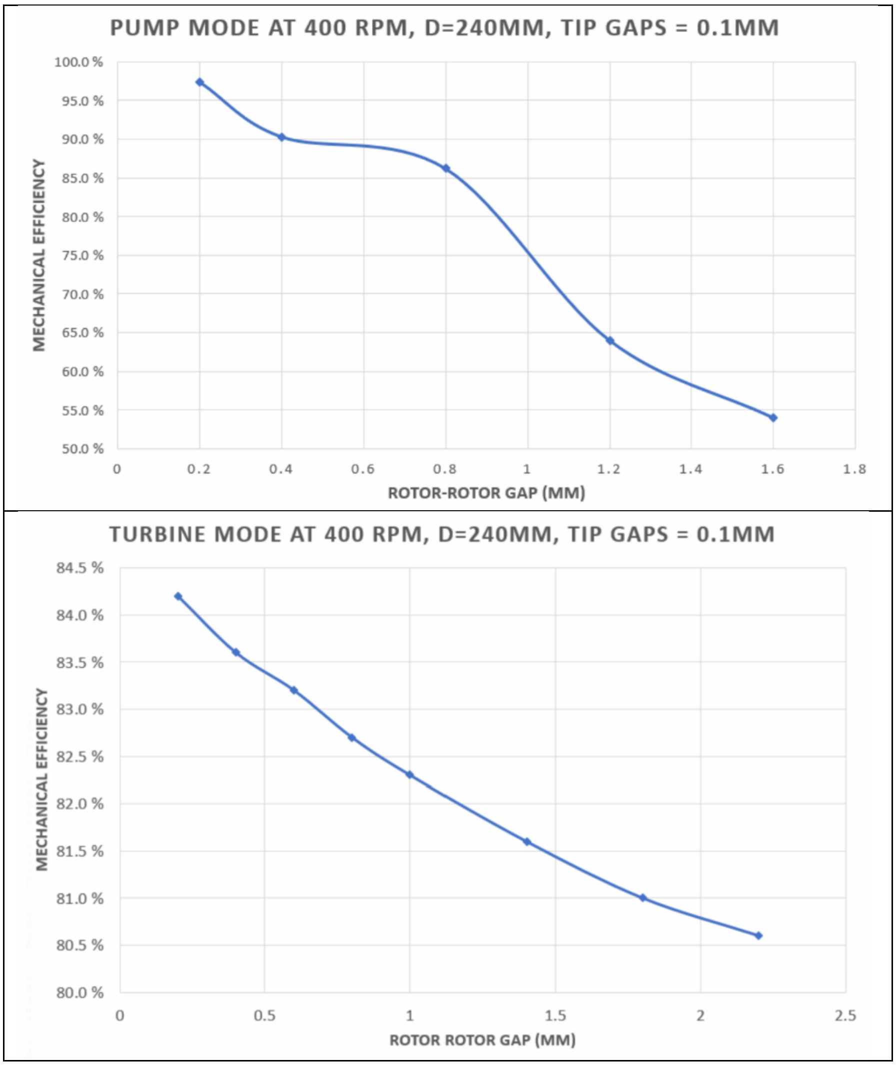

Figure 21 – Rotor-rotor gap optimization study for pump and turbine mode at 400 rpm

Previous works to ALPHEUS have tested different gap sizes between rotors for a prototype scale to check its influence over the turbine efficiency when a water head of 2m and a rotation speed as low as 16 rpm is applied. The gap was changed by applying different outer lobe sizes from a circular profile, resulting in a different rotor diameter with a fixed centre to centre distance. The three gaps tested were 5, 10 and 20 mm. The results are presented in Table 5.

Table 5 – Effect of the gap size between rotors in turbine mode

Gap size between rotors	Torque [Nm/m]	Power [W/m]	Mass flow [kg/sm]	Efficiency [%]
5 mm	7,915	13,262	1,359	49.7
10 mm	10,304	17,265	1,337	65.8
20 mm	11,277	18,895	1,430	67.4

The highest efficiency for the prototype scale was obtained with a 20mm gap, indicating that a peak of efficiency could be found when the rotor-rotor gap was increased up to a certain value.

Such conclusions contrast with the latest findings, but the applied methodologies were different. First, two different rotor profiles were tested (cycloidal vs circular). Second, in one case the fixed parameter was the rotor diameter while in the second case the center-center distance was the one that did not change.

Since a new machine will be implemented at TU Braunschweig in order to test turbine mode and check for overall efficiencies, another 2D CFD is implemented to analyse how big the rotor-rotor gap should be for the new rig. The following images and results show the efficiency curves for turbine mode when a cycloidal profile is used, rotor-rotor centre distance and tip gap are fixed, while rotor diameter and rotor-rotor gap vary. It can be seen that a smaller rotor-rotor gap also generates better efficiencies. Therefore, the differences between those works should probably rely on the use of different rotor profiles and different rotation speeds.

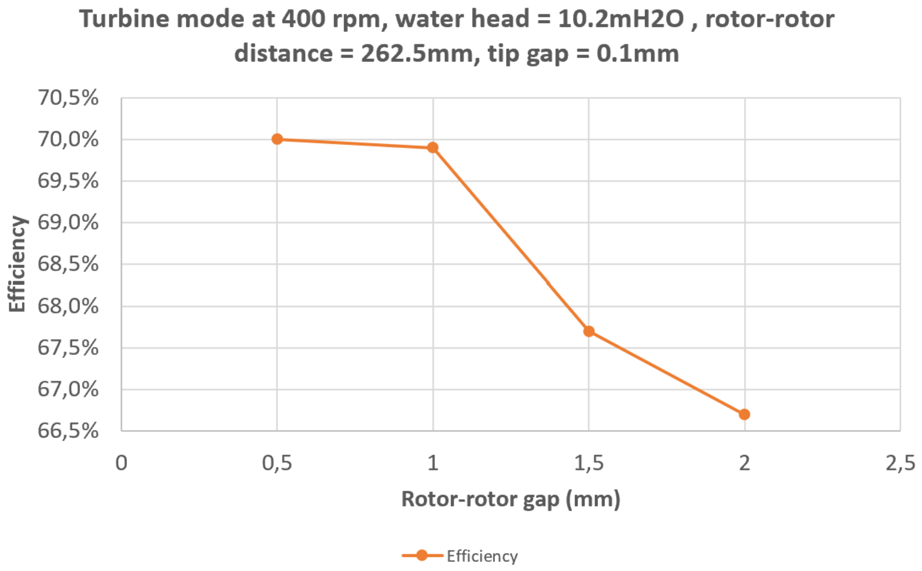

Figure 22 – Rotor-rotor gap optimization study for TU Braunschweig rig.

6.4 Twisted rotors

Kurokawa et al. (2008) explain that in order to reduce pressure pulsation, one can install a small sized simple surge tank at the inlet and outlet of the turbine, and that could reduce the pulsation amplitude by 75%. However, it should be possible to reduce pulsation without installing supplemental (and expensive) structures. That is one of the reasons why the authors studied a pair of four-lobe type rotor twisted helically with a twist of 11^{o}, and they compare it with a three-lobe rotor. The authors explain that pressure pulsation increases remarkably with an increase of rotational speed and differential pressure in a three-lobe straight type PD turbine. On the other hand, the twisted rotors reduced pressure fluctuations to about 20% of that of the straight three-lobe rotor. As the helical lobe presents a bigger surface area, leakages are expected to be higher through both tip clearances and centre clearances. Torque and leakage are almost dependent only on the differential pressure, same as the straight 3-lobe type, but torque efficiency becomes much higher.

Sonawat et al. (2021) say that machines that suffer of large pulsations in the flow can cause generation of noise, vibration and fatigue, leading to structural damage or breakdown of the device. So, they suggest the use of twisted rotors in order to damp most of the flow fluctuations. Sonawat et al. (2020) had a special look at the occurrence of cavitation in PD turbines by doing multi-phase CFD simulations, and they showed that the utilization of a 45^{o} twisted rotor could practically eliminate the occurrence of cavitation because the contact area of the fluid for both rotors was uniform irrespective of the orientation or rotation of the lobes. Hence there was no abrupt change in the fluid properties. On the other hand, the 45° twisted rotor produced 1.15% less theoretical hydraulic efficiency compared to the straight lobe design due to increase in the leakage losses associated with it. But a vibration free device might ensure a better longevity of the machine, which also can reduce maintenance costs.

Thus, in the second run of PD RPT experimental tests in ALPHEUS, a straight lobe might be the primarily chosen design in order to try to maximize the efficiencies and compare the solution with other technologies such as the Contra-Rotating RPT (CR RPT). Although, a twisted rotor PD RPT should also be considered and investigated in a final solution that includes fatigue, lifespan and costs of the machine.

6.5 Other design parameters

Seiche and wave phenomena are mentioned in the task description. Monitoring this will be important for the implementation phase at an actual site with known depth and shoreline profiles. It is highly dependent on local characteristics, and it turned out not to be possible to include in a general way in this report. A site-specific investigation must be carried out for all projects.

As we could see through this report, the presence of recirculation areas increases the pressure drop in the system and affects the flow rate and the generated power. Thus, by including a feature that provides a smoother transition and eliminates the recirculation areas, such as the diffusor utilized in the Chalmers experiment, could generate higher efficiencies and output power. The proposed final design for the measurements at TU Braunschweig includes a transition from circular to rectangular shape with a constant cross-sectional area.

Another suggestion presented by project advisor RONAMIC is the reduction of the total mass in the rotors. We can keep the same rotor surface profile while reducing its weight and costs in material, without affecting its structural properties. Moreover, the reduction in weight can provide more flexibility regarding the rotation speed, torque and operation conditions.

6.6 Optimal design for TU Braunschweig rig

The next PD RPT machine will be built in TU Braunschweig and that design has followed the conclusions from this section as much as possible in terms of construction decisions and design optimization.

The new design will contain two rotors with cycloidal profiles and diameters of 348.67mm, rotor height of 300mm, tip and side gaps equal to 0.15mm, and rotor-rotor distance of 262.5mm. A circular pipe of 300mm of diameter will transition in shape to a rectangular profile to match the rotors height, and the inlet width is therefore 235.62mm. The maximum designed output power is 15.34kW when rotating at 500 rpm, maximum torque supported by the motor is 293 N.m., and the maximum flow rate provided by the system is 325 litres per second. Figure 23 shows the designed concept.

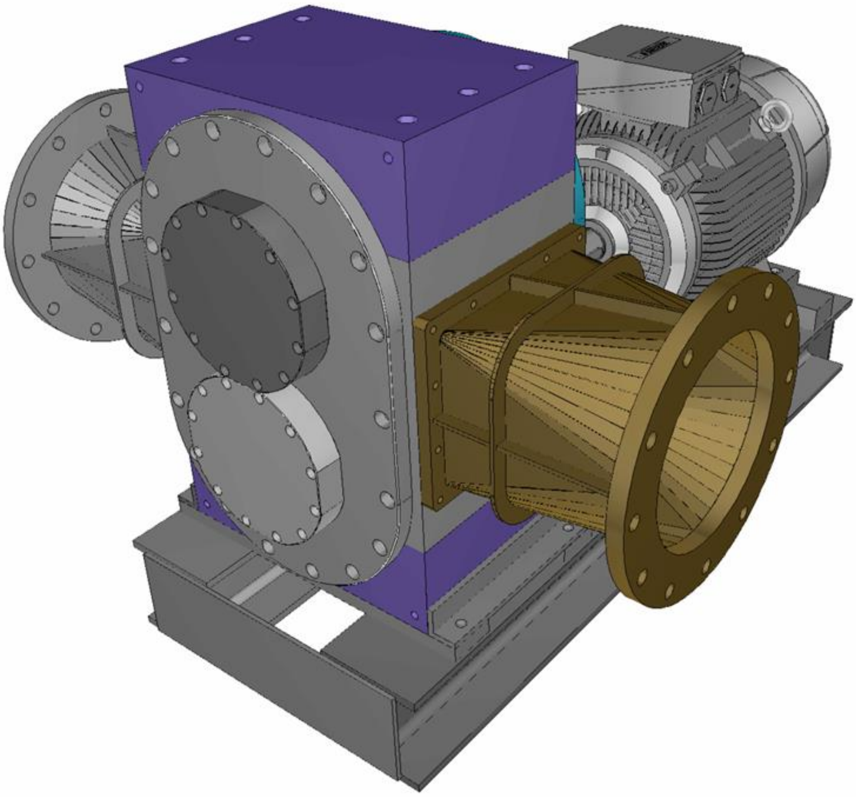

Figure 23 – Positive displacement reversible pump turbine designed for TU Braunschweig.

2D simulations were performed to estimate the power output, efficiencies, torque and pulsation levels for the TUB unit. A net water head of 7.8m is estimated. Three-dimensional effects and mechanical losses in transmission should decrease generated power and mechanical efficiency. Figure 24 and Figure 25 show the maximum expected turbine mode efficiencies, power output, and average flow rate as function of the rotation speed.

With a straight lobe design, pulsation could be observed in all controlled parameters, and they are greater for lower rotation speeds. At rotation speed of 100 rpm, power and flow rate presented 10% and 11,5% of variation, respectively. At 600 rpm, power and flow rate present 7% and 6,5% pulsation levels respectively.

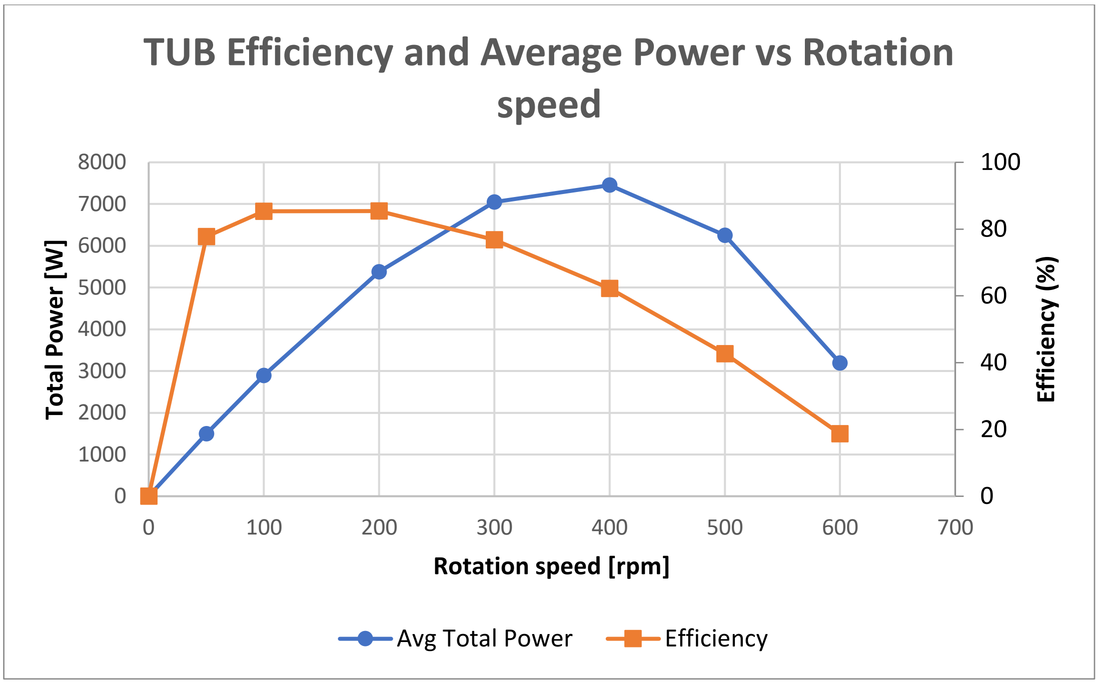

Figure 24 – Efficiency and average power curves vs rotation speed for the TU Braunschweig unit in turbine mode.

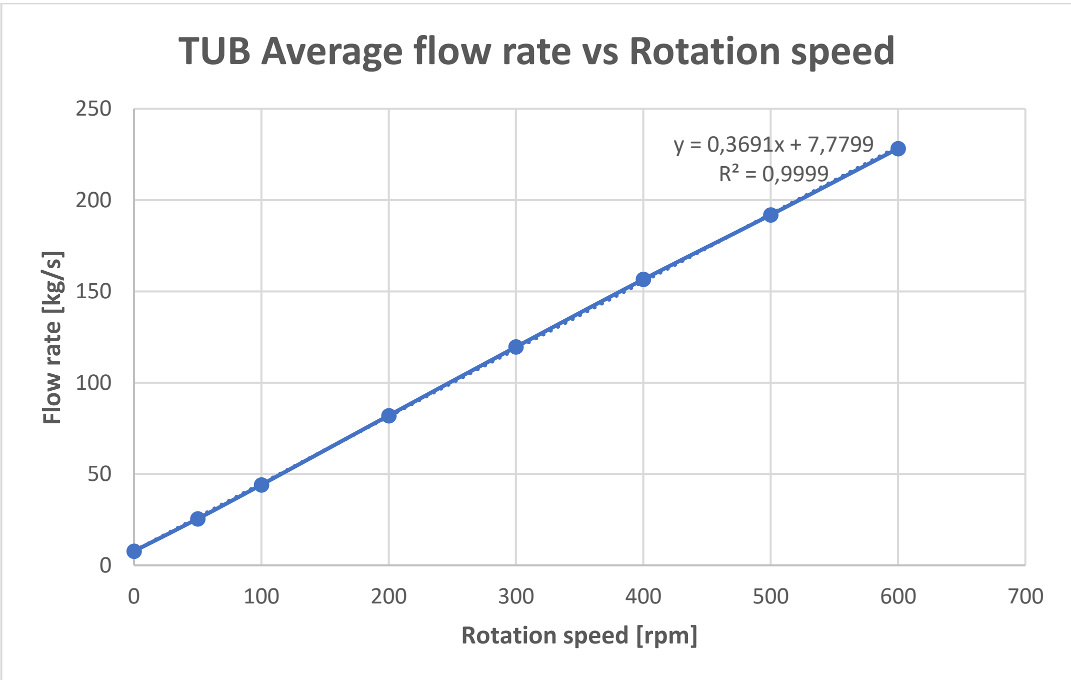

Figure 25 – Average flow rate vs rotation speed for the TU Braunschweig unit in turbine mode.

From Figure 24 we can see that the maximum efficiency is expected to appear between 100 and 200 rpm, and it is slightly above 85%, while the maximum average power equals to 7000 W if the machine is running at 400 rpm. Figure 25 shows a linear relation between flow rate and rotation speed, and it shows a constant leakage value of approximately 7,78 kg /s for a water head of 7,8m.

7 Fluid Structure Interaction (FSI)

By using the designed PD RPT device for TU Braunschweig, a one-way fluid-structure (FSI) simulation was performed to estimate the stresses and deformation magnitudes on the rotor. An aluminium alloy was chosen as material reference.

First, the pressure distribution on the rotor surface was retrieved for the angle position that provided the maximum torque appearing during a full turn. A static structural analysis was then prepared where the rotation velocity and a cylindrical support were included as constraint, and the CFD calculated surface pressure was assigned to the rotor surface.

Figure 26 shows the Von-Mises stresses in a rotor running at 300 rpm, and Figure 27 shows the total deformation for the same case. As can be seen, the maximum stress occurs close to the shaft while the highest deformation happens in the tips of the lobes. As shown, the maximum stress was lower than 1 MPa and the maximum deformation was lower than 1 µm. Those values are too small to bring up any concerns on structural safety of the device. Other phenomena such as cavitation should be studied to verify the life span of such machine.

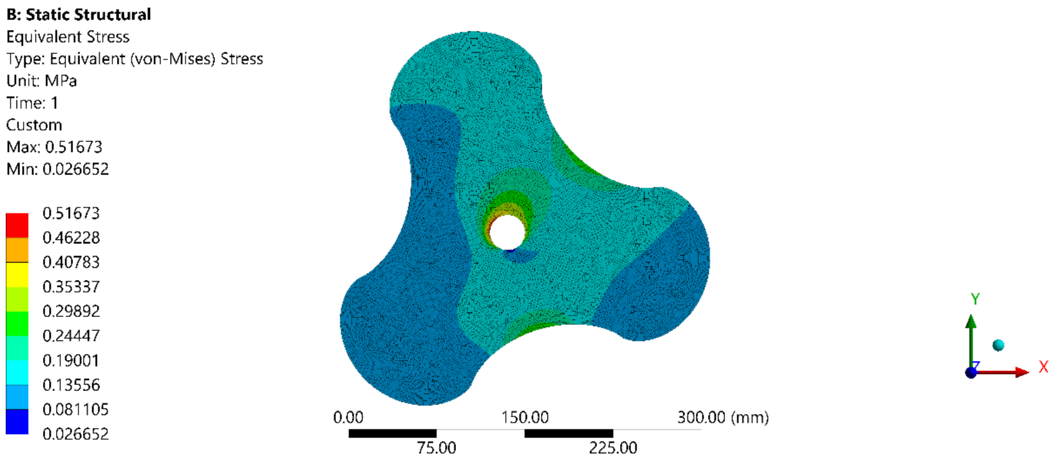

Figure 26 – Von-Mises stress for turbine mode at 300 rpm.

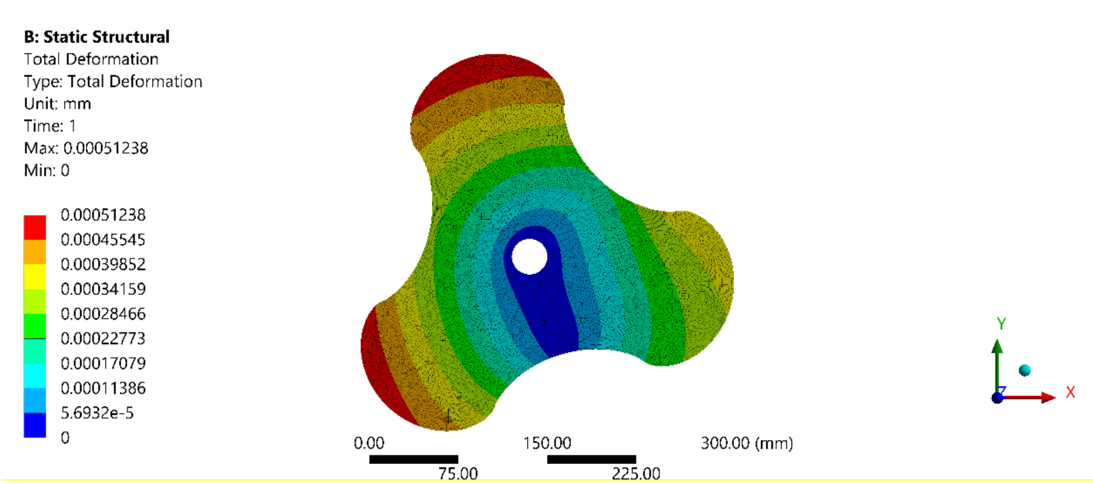

Figure 27 – Total deformation for turbine mode at 300 rpm.

8 Fish mortality and design optimization

Looking into fish mortality is a key element of ALPHEUS as the intention is to promote fish friendly designs. Including fish mortality into the design optimization will involve many uncertain parameters and unknowns, too many for the Alpheus project to be able to conclude in a useful way. We will however outline a methodology that can be used as well as providing an example of one such optimization. The limits, numbers and so on used to quantify probabilities and mortalities in this section is taken from ALPHEUS D2.6, the report: "Fish mortality to be expected from prototype scale turbine", unless given a footnote.

The methodology starts by identifying target species for the analysis, species that are relevant for the location of the project. The key is to identify the fish size, which will vary depending on species and the life cycle, possibly as well on sex. The analysis is then performed for each operational mode and relevant fish lengths. For each species/sex/life cycle period the death of one specimen must be assigned a monetary cost, K. What this cost might be is likely to vary between species, rare and endangered species are likely to have higher cost than species that are abundant. If there is no cost linked to the death of specimen, there is no incentive for trying to keep them alive and it is pointless to optimize including fish mortality in the analysis as it is given no weight at all.

The basic idea used to be able to include fish mortality into the design optimization is that the cost of the fish mortality must be covered by the revenues generated by the operation of the unit. Multiplying the cost of one casualty with fish mortality rate and dividing this by revenues generated per unit electricity we get a parameter, P, which has the unit 'power' (kW], seen in the equation below;

$$P = \frac{Kn}{€}\ [W]$$

Where K is the cost of fish mortality (€ cost per one dead specimen), n is the mortality rate (dead specimen per time) and F is the revenues generated per unit electricity (€ per kWh).

The interpretation of this is that P is the amount of power required to generate revenues that will cover the cost of the dead fish. This power is occupied from the operation and can be deducted from the output power (the numerator in the efficiency for both pumping and generating mode) as a loss of power. When fish mortality rate is linked to characteristics dependent on the design parameters of the unit an optimization of the efficiency where the power P is included will result in a design where fish mortality is taken into account.

In the case of a pumped storage power plant the revenues generated per unit electricity it is the price difference between selling price and buying price, as the water for generation must have been bought and pumped before being able to generate and sell electricity. Efficiencies must also be taken into account, and for the pumped storage power plant the cycle efficiency must be used. This will typically give a circular reference in a numerical scheme (finding the efficiency will partly be dependent on the efficiency itself) so a fixed and representative value is considered to be acceptable.

We must identify and describe the fish mortality rate, n, in detail. We can't predict the death of individual specimen, however it's likely that we can regard them as stochastic variables and find the probability of the fish mortality rate. We assume now that the mortality is linked to the transportation of fish through the unit and choosing female mature adult atlantic eel (Anguilla Anguilla, rarely larger than 1 m, females bigger than males[3]) as the target species, we can identify three causes for mortality during the transportation in generation mode;

a) Strike and grinding: Eel being hit and grinded by the rotating part and suffering injuries and subsequent death
    a. The probability of fish *m*ortality due to *s*trikes, P(*ms*), is the probability of fish being struck multiplied with the probability of being killed by a strike

$$P(ms) = P(ks)P(s)$$

Where P(s) is the probability of being struck and P(ks) is the probability of being killed by a strike, P(ks).

i. Probability of strike P(s) can be assessed using several probability functions described in Alpheus D2.6, however developed for fish passing thorough turbomachinery in generating mode and not positive displacement machines. The function by Hecker and Allen, 2005 for the probability of fish striking the structure, P(s), is the time it takes for the fish to move its own radial length component divided by the time is takes before the rotor to move the length of the distance between two blades:

$$P(s) = n(Lsin\alpha)\frac{z}{V_r}$$

Where n is the rotational speed (rps), z is the number of blades, L is the fish length in meters, α is the inlet absolute flow angle, Vr is the radial velocity. Adopting the concept of ratio of the time it takes for the fish to move its own length to the time it takes for a blade passage to pass to the PD machine geometry and action, we can put up the expression

$$P(s) = \frac{{LRZ_{lobe}}/{Q}}{\frac{2\pi R}{6\omega R}} = \frac{6LRZ_{lobe}n}{Q}$$

Where the assumption in that the fish is coming in tail (or head) first at the velocity of the average oncoming flow. For the optimization procedure we are likely to be looking at cases where the rotor is rotating so fast that theoretically all fish are struck. Even higher rotational speed are possibly investigated and P(s) will in this case be higher that one, which is very wrong use of a probability. We solve this by looking at the cumulative normal distribution using an upper limit of the above P(s) as the value where the cumulative distribution is very close to 1. For this example, we will use

$$\frac{6LRZ_{lobe}n}{Q} = 1{,}5$$

[3] https://en.wikipedia.org/wiki/European_eel

as the value where the cumulative normal distribution is 0,99 (Result in normal distribution given by μ=0,75, σ=0,323). Using this value of 1,5 we are taking into account some of the forgiving effects by the replacing action sucking fish in with a higher velocity that the average oncoming flow as well as all fish not being oriented tail (or head) first. The cumulative probability function we use is therefore

$$P(ks) = P_{cnd}(\frac{6LRZ_{lobe}n}{Q}; \mu = 0{,}75; \sigma = 0{,}323)$$

Where the subscript cnd is an abbreviation for Cumulative Normal Distribution.

ii. The probability of being killed by the strike, P(ks) must be found. A safe limit of 5 m/s where limited or no fatalities occur has been reported in case of some species, and this is used in the example here as well. Here emerges another benefit of using the normal distribution as well, namely the possibility of defining a lower value which result in zero probability values less that this limit. The safe limit of 5 m/s is used as such lower value. A strike velocity of 10 m/s is at the same time reported likely to be lethal, and we will use this as the upper limit for the cumulative normal distribution equal to 0,99 (Result in normal distribution given by μ=7,5, σ=1,085).

$$P(ks) = P_{cnd}(\frac{6LRZ_{lobe}n}{Q}; \mu = 7{,}5; \sigma = 1{,}085)$$

b. Grinding between casing and rotor is not assumed to be very relevant as the technical efficiency suffers hard for increasing gap clearances and the gaps that give acceptable technical efficiencies are too small for eel fitting in there, as well as in generating mode the gap travels away from the fish in the direction of the leakage and the eel will not be squeezed between structures. This is true for the rotor-rotor gap as well in generating mode.

b) Eel being cut by the rotor as this passes the casing inlet geometry
   a. If the eel is sucked into the lobe by the replacing action it will be moved towards the casing inlet geometry with the rotor speed, by the rotor. This means that the probability of *m*ortality due to *c*utting, P(*mc*), by the inlet casing geometry can be assumed to be the same as the probability of being struck by the rotor

$$P(mc) = P(s)$$

c) Fish being injured by large shear forces and turbulence when caught between the lobes of the rotor and carried through the machine, mostly linked to early stages of life where the fish size is small
   a. A strain rate of less than 500 s^{-1} is considered safe to juveniles, and fish of bigger size is typically not affected much. We well therefore not include this in the analysis.

b. Turbulence is affecting fish first when the eddy size is in the scale of the fish size. The scale of the eddy inside the lobe volume will be R/2, since this is the radial distance from the lobe volume at its smallest radius to the casing. The mechanisms for mortality linked this turbulence is fish disorientation (susceptible of increased predation), compression and distortion. The intensity of the vortex is clearly a parameter. “Hydrokinetic turbines lacking structures leading to and from the rotors or blades (e.g. stay vanes, wicket gates, draft tubes) and operating in conditions of low velocity and little change in flow direction would have lower likelihood of occurrence of turbulence-related injury (EPRI, 2011)”. (Ref ALPHEUS report D2.6) This is in favour of the PD machine. Still, it’s likely that high rotational speeds causing a large eddy inside the lobes and rotor diameters in the size of the fish will have an effect, and to have the effect included in the analysis we make the assumption that the higher rotation of the eddy (which theoretically rotates three times the rotational speed of the rotor, but in opposite direction) as well as fish length to lobe size (R/2) will be the important parameter. Setting limits to this parameter is not easy as no numbers of any kind are given in the report ALPHEUS D2.6, but setting the limit for no mortality of the parameter 6ωL/R to 5 and the upper limit as 15, The probability function for the _m_ortality due to _t_urbulence, P(_mt_) is the cumulative normal distribution for the parameter 6ωL/R with a mean μ=10 and a standard deviation σ=2,12

$$P(mt) = P_{cnd}(6\omega\frac{L}{R}; 10; 2{,}12)$$

We don’t expect fish to be squeezed by the displacing action of the rotors as the fish have close to neutral buoyancy and the pressure gradient in the water during the displacement action would also displace the fish themselves.

The three points above assumed to be the reason for fish mortality are a part of a sequence. The likelihood of fish dying due to collisions with rotation parts (point 1) will give an expectation of how many fish will die, and subsequently there are fewer fish that can die by being cut in parts by the second mortality cause. The expected value of the number of fish dying at this location will reduce the number of fish that can die due to the last cause of mortality. The mortality rate for each steps can be summed into a total mortality for the unit, and this is presented in the result as a percentage of the fish entering the unit.

For pumping mode, the analysis on mortality of mature female European eel can be quite simple; no-one is returning because they die after spawning. In case the eels stay in the region close to the PD machine they might be pumped up again, migrating more times through the unit and being subjected to mortality in both pump mode and generating mode several times. This analysis will however be too complex for the purpose of this report. Therefore, the assumption is that there is no mature female eel mortality in pumping mode.

8.1 Case for optimizing design including fish mortality

The fish length has been set to L=1m, and fish density has been set to 0,000001 mature female eel/m3, corresponding to one eel in an Olympic size swimming pool (~1Mm3). The revenues generated per unit electricity is set to 0,15€/kWh, and the cycle (technical) efficiency is set to 0,9.

The cost of fish mortality was set to 1000€. The result is seen in Figure 28.

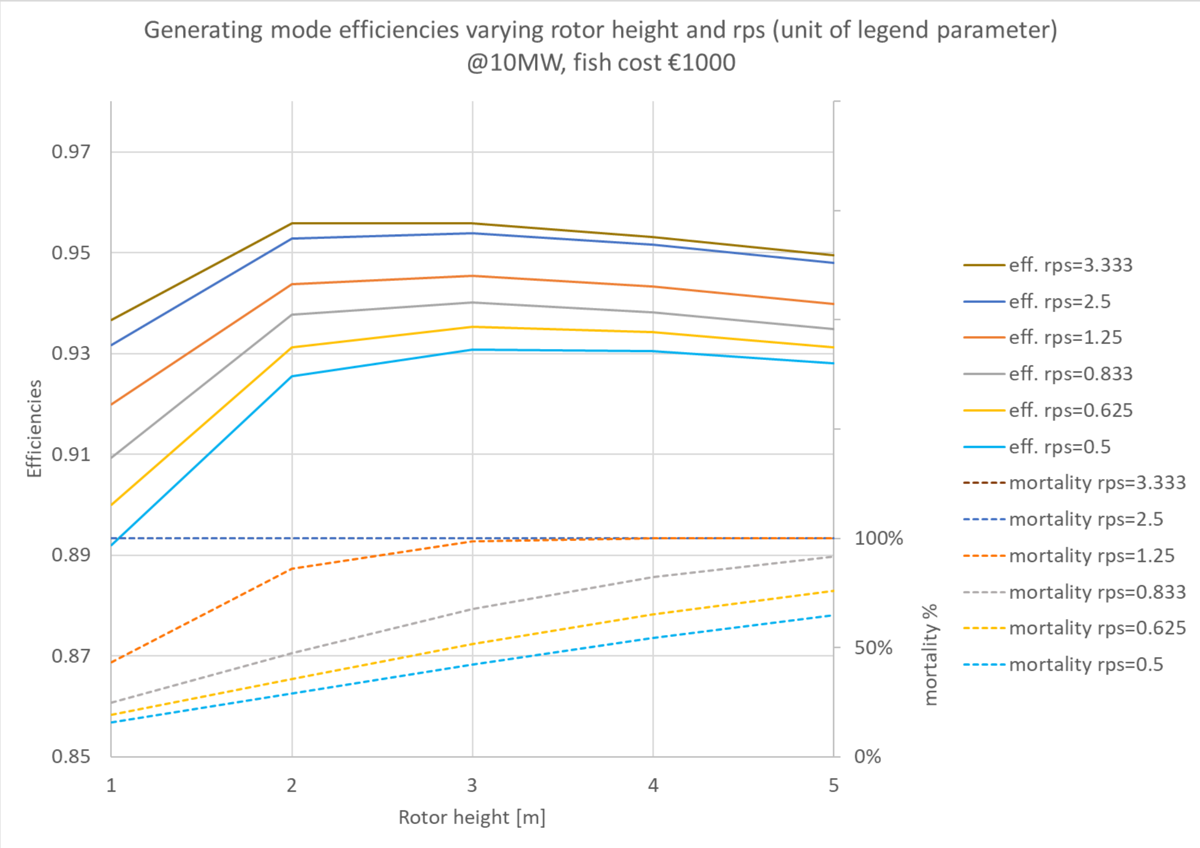

Figure 28: Generating efficiencies analyses using fish mortality unit cost of 1000€

We see that low rotational speeds and low rotor heights does reduce the fish mortality, but the effect on the efficiency is not big enough to favour designs that reduce fish mortality by increasing the efficiency. As no cost have been added to the pumping mode a cycle efficiency analysis will effectively end up with the same design as with no cost due to fish mortality. (Synchronous speed: 500 rpm (8,333 rps) , rotor diameter: 2,814m, Rotor height: 3 m), 100% fish mortality and a small efficiency penalty with a cycle efficiency <92,13%.

A cost of 10000€ was then used, and this high cost resulted in so big penalty on the efficiency that the peak efficiency point moved towards designs favouring less fish mortality, which can be seen in Figure 29.

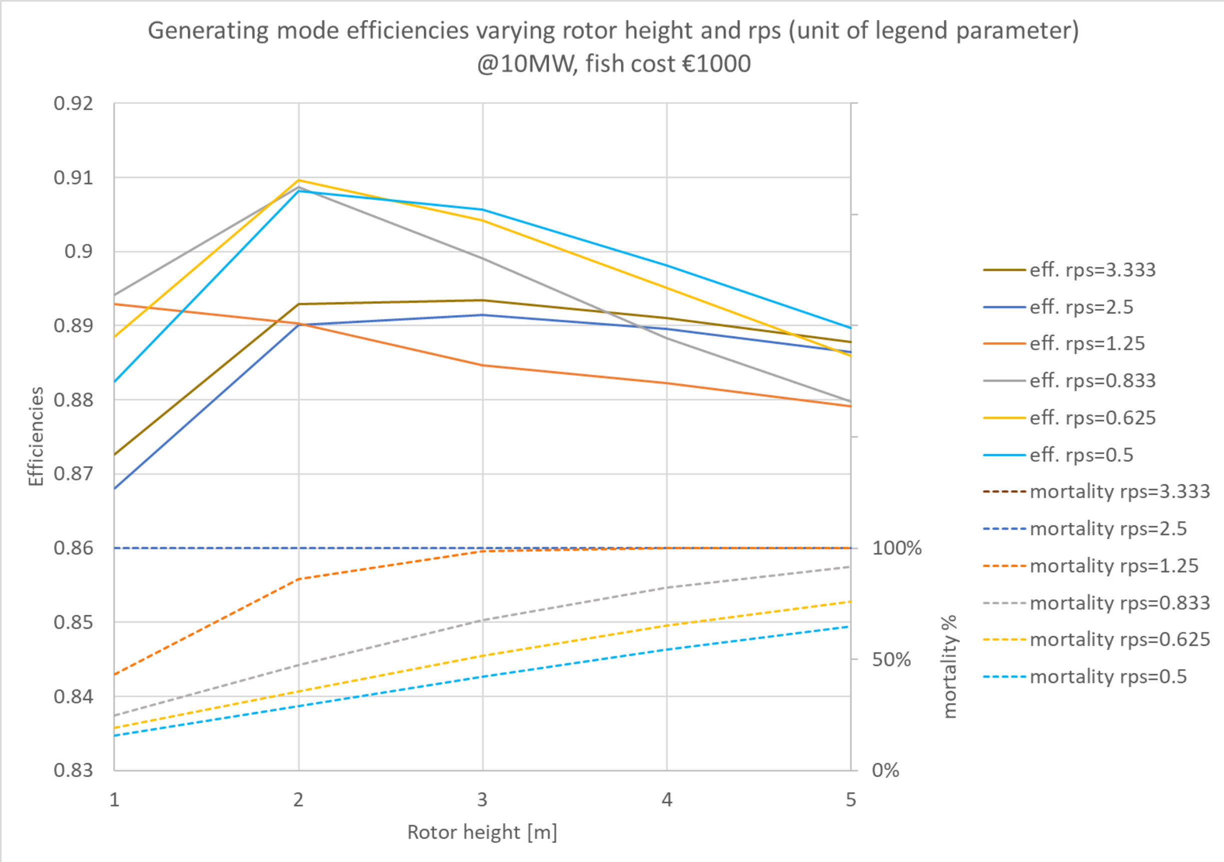

Figure 29: Generating efficiencies analysed using fish mortality unit cost of 10000€

Figure 29 is showing that for the higher rotational speeds the mortality is still 100%, and the efficiency low (and shaped like the previous efficiency curves) due to the penalty coming in full for these designs. At a rotational speed of rps=1,25 things have started to happen and efficiency shifts for the lower rotor heights (lower rotor height imply a larger radius and the eel begins to fit in between the lobes and not being killed by strikes and cutting). The effect on the efficiency is observed for the rotor height Z=1 at rps=1,25. This efficiency shift is observed for rps=0,833 as well, but occurring at higher rotor heights as the lower rotational speed itself has increased the rotor diameter. The efficiency curve for rps=0,625 is actually obtaining a local maxima at Z=2. The fish mortality has dropped from 100% to less than 50% for Z=1 going from rps=2,5 to rps=1,25.

The full effect of the optimization is seen to play out for the lower rotational speeds, resulting in identifying candidates for performing the cycle efficiency in order to look for the optimal design at highest cycle efficiency. The result from the analysis for the cycle efficiency for operation between H=5m and H=10m is shown in Figure 30:

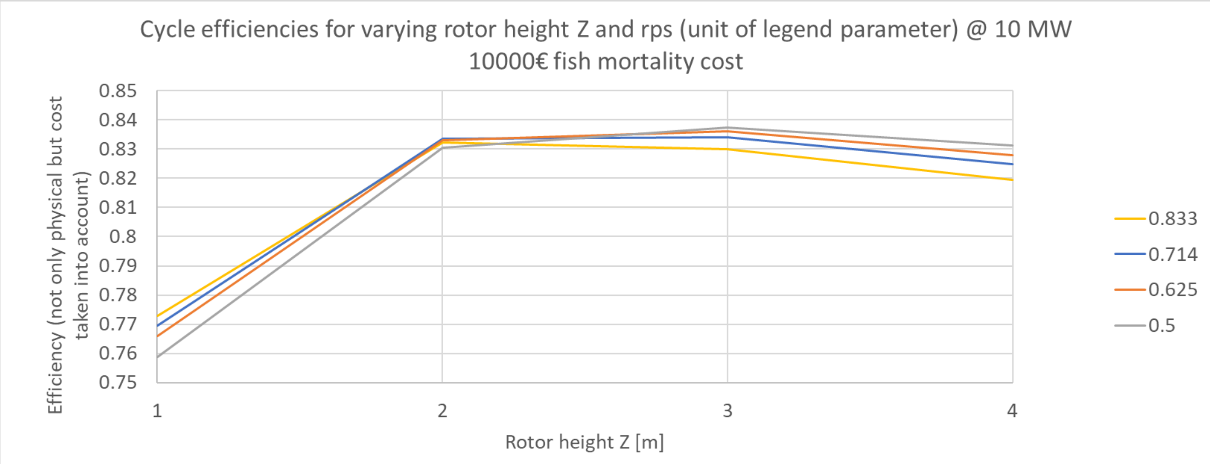

Figure 30: Cycle efficiency for the case of fish mortality cost of 10000€

As seen in Figure 30 there is no peak value obtained, as the efficiency is not found to drop off. The search was however aborted, as the rotor diameter for the maximum efficiency value in Figure 30 (rps= 0,5 and a rotor height of Z=3m) is D=11,49m. The fish mortality of this design is 42%. The rotors of such unit would make the unit span more than 20,1 m, and it's hard to think that the cost of such unit (taking both rotor and generator dimensions (generator having 100 pole pairs) into account) will result into a project which is financially sound through a techno-economical optimization likely to favour much lower rotor diameter due to cost of construction and equipment.

In this particular case with long fish one solution could be to increase the installed capacity of the unit. In fact, keeping the dimensions at D=11,49m, Z=3m but doubling the installed capacity and doubling the rotational speed would only increase the mortality by 3% points, from 42% to 45%, and represent a much higher potential for generating revenues. In a more comprehensive techno-economical optimization the installed capacity of the unit should be a parameter as well and would lead to the best design in a larger frame, including cost of construction as well as the effect on fish mortality.

The conclusion of this section must be that the fish mortality for a positive displacement reversible pump turbine as investigated by ALPHEUS is still unacceptably high for the longer fish specimen (~1m) that's found in coastal regions and shallow waters.

Measures for avoiding, in this case, the long mature female eel to pass through the unit might turn out to be a much better solution than trying to have them survive this passing. This is outside the scope of this report, but still an important thing to note.

9 Conclusions

The report presents a multidisciplinary optimization of two different sized PD RPT units, one at a lab scale where disciplines involving hydraulics and structural analysis has been combined, and one at a 10 MW unit where disciplines involving hydraulics and biology has been combined.

Shown is the development of an analytical model for a PD RPT machine used to find the optimal main dimensions of a 10 MW unit operating at head between 5 and 10 meters. ***The analytical model is partially verified using CFD simulations.***

The CFD simulations are compared to experimental results obtained on a small-scale test rig at Chalmers University of Technology using high-fidelity measurement techniques obtaining detailed information about the flow field. Based on this, ***the CFD model is considered to be valid***.

The CFD model is used to find an optimal design for a test rig to be constructed at TU Braunschweig, and results from this will be used to further validate the analytical model. The CFD model is linked to investigations in the structural domain and ***based on the stresses and deformations at maximum torque there is no concern for the structural integrity of the TU Braunschweig unit***, complying to the material properties of the analysis.

The analytical model is extended to include fish mortality and the effect this has on the overall efficiency of the unit, given a cost of dead fish specimen and the subsequent power that is occupied during operation to provide the revenues to cover the cost. The fish mortality rate is found using a probabilistic model linked to the main dimensions of the unit. This enable the search for an optimal efficiency where fish mortality is considered, leading to less fish mortality if the cost of dead specimen is sufficiently high. However, ***the concept of a PD RPT machine used as a fish friendly alternative for energy storage is not supported by this analysis for the longer (>~1m) fish species found in coastal areas***. Other measures for reducing fish mortality than designing the units for safe fish passage should be investigated, at least for the longer fish species.

10 References

J. Kurokawa, J. Matsui, Y.-Do Choi, Flow Analysis in Positive Displacement Micro-Hydro Turbine and Development of Low Pulsation Turbine, International Journal of Fluid Machinery and Systems, 2008, Volume 1, Issue 1, Pages 76-85, Online ISSN 1882-9554, https://doi.org/10.5293/IJFMS.2008.1.1.076

D. Phommacchanh, J. Kurokawa, Young-Do Choi, Noboru Nakajima (2006). Development of a positive displacement micro-hydro turbine. JSME International Journal, Series B, Vol. 49, No. 2, pp. 482-489. doi:10.1299/jsmeb.49.482

J. Schiffer. A comparison of CFD-calculations and measurements of the fluid flow in Rotating Displacement Pumps (2012). International Rotating Equipment Conference 2012, Düsseldorf.

A. Sonawat, Y.-S. Choi, K.M. Kim, J.-H. Kim, Parametric study on the effect of inlet and outlet pipe shape on the flow fluctuation characteristics associated with a positive displacement hydraulic turbine (2021), Renewable Energy, 163, pp 1046-1062, ISSN 0960-1481, https://doi.org/10.1016/j.renene.2020.09.025.

A. Sonawat, S.-J. Kim, H.-M. Yang, Y.-S. Choi, K.-M. Kim, Y.-K. Lee, J.-H. Kim, Positive displacement turbine - A novel solution to the pressure differential control valve failure problem and energy utilization, (2020), Energy, 190, 116400, ISSN 0360-5442, https://doi.org/10.1016/j.energy.2019.116400.

Y.-H. Kang, H.-H. Vu and C.-H. Hsu (2012). Factors Impacting on Performance of Lobe Pumps: A Numerical Evaluation. Journal of Mechanics, 28, pp 229-238 doi:10.1017/jmech.2012.26

11 Appendix: Analytical Model of Positive Displacement pump

A1 Introduction

This document is presenting analytical work resulting in a model for the efficiency of a Positive Displacement pump. Subject to careful investigation of the signs of different terms included in the efficiency it is possible to use it as a model for the efficiency of operating in generating mode as well. The public document Deliverable D2.4 in the EU funded ALPHEUS[4] projects is presenting the model described herein applied to the operation in both pumping and generating mode. The ALPHEUS project has also funded the work on this analytical model.

References are intentionally not used in this document as the goal has been to develop the expressions from first principles, or at least scientifically accepted applications of first principles. As a general reference publication fourth edition in SI unit of “Fluid mechanics, fundamentals and applications” by Çengel and Cimbala (McGraw Hill) can be used.

A1.1 Schematics of the Positive Displacement machine

Figure 31 and Figure 32 is showing the schematics of the Positive Displacement (PD) machine. The machine consists of two rotors that rotate “into” each other, bringing fluid from one port trapped between the rotor and casing and transported to the other port by the two rotors displacing the volume. This section will work on describing the flows and torques which occur at the gaps, and these gaps are indicated in the figures.

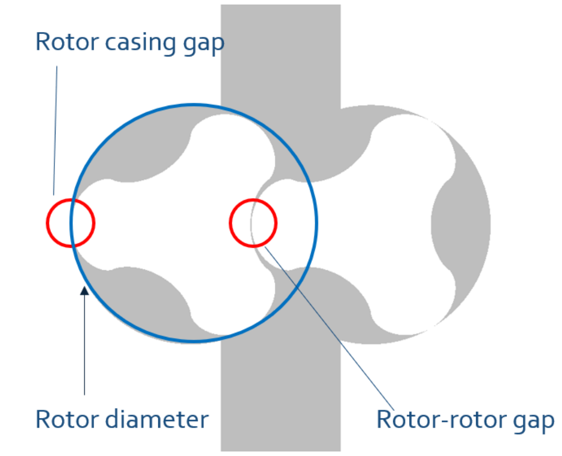

Figure 31: Top view of a Positive Displacement machine (Graphical elements by Luiz Gans)

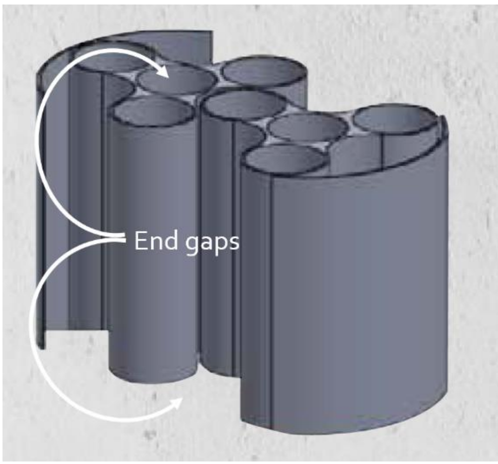

Figure 32: Side view of a Positive Displacement machine (Ronamic)

The analysis will be performed by investigating the left side rotor in Figure 31 sometimes referred to as Rotor 1, and then multiplied by two to get the performance of the two rotors. Their operation is phase shifted, but their average values are the same due to symmetricity. The high head side is the upper port in Figure 31, thus, pump mode operation will imply rotation in the clockwise direction of the left rotor.

[4] Grant agreement #883553

A1.2 Theoretical basis for the model

The basic initial assumption for this work is that we can use laminar theory to develop the functional relationship between the parameters that make up the problem. For increasing scales, we know that the laminar theory is incorrect as flows become turbulent. We will deal with this by scaling by the application of a one-seventh power-law velocity profile, described by

$$\frac{u}{u_{max}} = \left(\frac{y}{h}\right)^{1/7} \quad \text{[A1]}$$

A1.2.1 Application to shear forces

The laminar velocity profiles we will encounter in the analytical work are linear and parabolic velocity profiles. The gradient of the velocity profiles at walls are used to estimate torques or head losses, and the integral of velocity profiles are used to estimate flows. The linear velocity profile will result in a constant gradient,

$$\frac{\partial u}{\partial y} = \frac{u_{max}}{h} \quad \text{[A2]}$$

The power law profile differentiates as

$$\frac{\partial u}{\partial y} = \frac{u_{max}}{7h}\left(\frac{h}{y}\right)^{6/7} \quad \text{[A3]}$$

This is undefined at y=0, so we estimate it at as the velocity at a distance y=0,05h

$$\frac{\partial u}{\partial y} \sim \frac{u(0{,}05h)}{0{,}05h} = \frac{u_{max}(0{,}05)^{1/7}}{0{,}05h} = 13{,}03\frac{u_{max}}{h} \quad \text{[A4]}$$

We see that the power law gives an estimate of the velocity gradient at the wall which is slightly more than 13 times that of the linear profile of the laminar assumption.

For the parabolic velocity profile, the velocity gradient at the wall becomes

$$\frac{\partial u}{\partial y} = \frac{1}{2\mu}\frac{\partial P}{\partial x}h \quad \text{[A5]}$$

With the maximum velocity at the centre as

$$u_{max} = -\frac{1}{2\mu}\frac{\partial P}{\partial x}\frac{h^2}{4} \quad \text{[A6]}$$

We get

$$\frac{\partial u}{\partial y} = -4\frac{u_{max}}{h} \quad \text{[A7]}$$

So, the power-law velocity gradient is 3,25 times that of the parabolic profile.

These correction factors are important for scaling shear forces to be more realistic. In practise we will find velocity profiles that are combinations of the linear and parabolic one. It's debateable if it will be correct to multiply both the gradients with these correction factors, or if the sum of them should be scaled up to the power law value. This is a pending question but for the future work the individual shear forces will be multiplied with their corresponding scaling factors.

Using the correct sign is often tricky when it comes to shear forces from differentiated velocity profiles. One trick is to evaluate the sign based on inspection of the flow driving or being driven by the solid boundary. This will be inspected for each case in the following work.

A1.2.2 Application to flows

When finding scaling factors for the flow we must integrate the velocity profiles. Integrating the laminar profile, we get a flow per unit area of

$$\frac{Q}{l} = \frac{u_{max}}{2} h \quad \text{[A8]}$$

Integrating the power law profile, we must remember that sometimes it's not actually the power law profile which is relevant for us because the flow is driven by the boundary and not limited by the boundary. The effect of this is that the velocity profile becomes

$$\frac{u}{u_{max}} = 1 - \left(\frac{y}{h}\right)^{1/7} \quad \text{[A9]}$$

we get

$$\frac{Q}{l} = u_{max} h - \frac{7u_{max}}{8} h = \frac{u_{max}}{8} h \quad \text{[A10]}$$

Which is one fourth of the linear one.

Integrating the parabolic velocity profile we get

$$\frac{Q}{l} = \frac{2u_{max}h}{3} \quad \text{[A11]}$$

When investigating the one-seventh power velocity profile we have to look at the original one, as the driver for the parabolic profile is the pressure gradients and the surface is limiting the flow. We must think of this problem as a symmetric problem around the centreline (y=h/2), where the velocity is maximum. Executing the integral we get

$$\frac{Q}{l} = \frac{7u_{max}h}{8\sqrt[7]{2}} = 0{,}7925 u_{max} h \quad \text{[A12]}$$

The correction factor will then be 1,18.

The same question regarding using both the corrections or correcting the sum of the linear and parabolic profiles persist for the flow correction as well, but regarding these two profiles as linked to separate key features of the problem (linear linked to rotation of solid surfaces and parabolic as linked to leakage flow due to pressure difference on each side of gaps), the correction factor should be used for both profiles so that the correction is still valid if looking at cases when there's no rotation or no pressure difference.

A1.2.3 The rotor-rotor gap position

The position of the minimum value for the gap between rotors is described by a so-called *lemniscate of Bernoulli*, closely resembling a figure 8, or an infinity sign. This geometrical feature is quite important for our case, as it will give us the basis for several things that we need in order to perform the calculations. The lemniscate is described by x(t) and y(t) coordinates given by

$$x(t) = \frac{\mathrm{a} \cdot \cos(t)}{sin^2(t) + 1} \quad \text{[A13]}$$

$$y(t) = \frac{\sqrt{2} \cdot \mathrm{a} \cdot \sin(t)\cos(t)}{sin^2(t) + 1} \quad \text{[A14]}$$

Seen below for a=R/2 and an offset in the x-direction by 3R/4, giving the lemniscate the correct trace for the gap of a PD machine where the rotor radius is R=3,55.

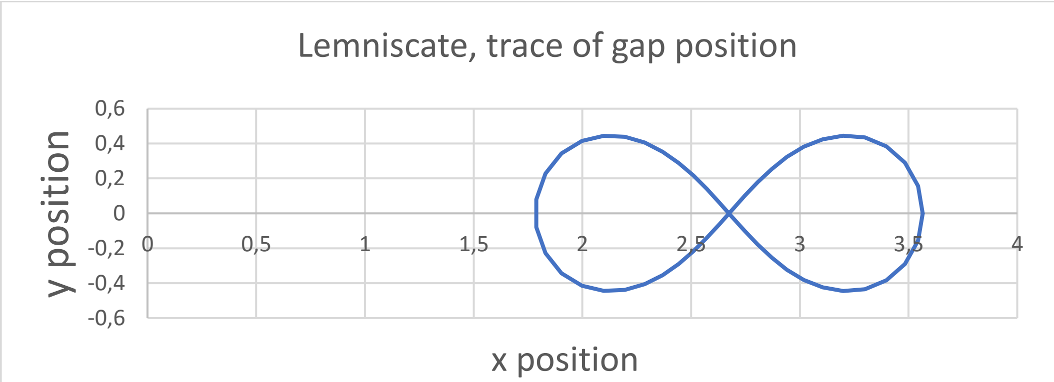

Figure 33: Lemniscate reproducing the gap trace

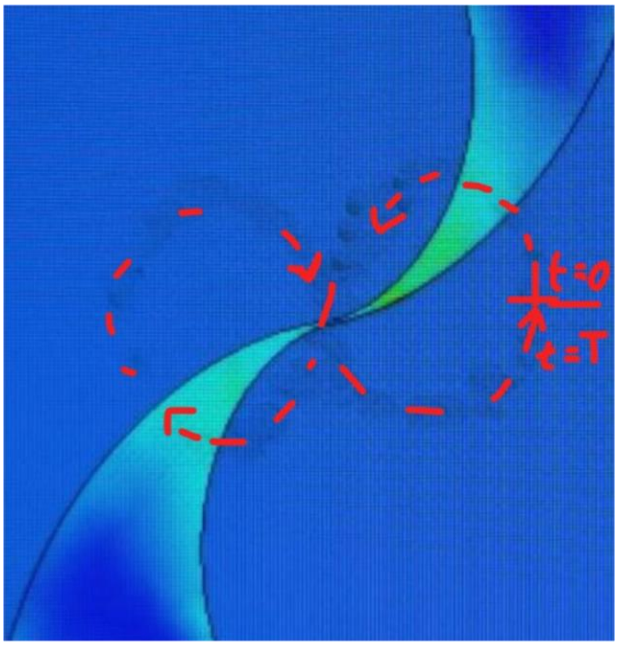

Figure 34: Leminscate draw onto a CFD image to outline the movement (CFD by Luiz Gans)

In Figure 34 the gap position has been manually traced as rotors rotate[5], and the red dashed line drawn to shown the direction of the movement. As we see the lemniscate is giving the position of the gap.

In some analysis we will need to know the velocity of the gap as it moves on the figure eight and this is found from the lemniscate trace parametric equations

$$V_{gap} = \sqrt{\left(\frac{dx(t)}{dt}\right)^2 + \left(\frac{dy(t)}{dt}\right)^2} \quad \text{[A15]}$$

The differentiation of x(t) and y(t) with respect to time yields:

$$\frac{dy(t)}{dt} = -\frac{\sqrt{2} \cdot \mathrm{a}(\sin^4(t) + \sin^2(t) + (\sin^2(t) - 1)\cos^2(t))}{(sin^2(t) + 1)^2} \quad \text{[A16]}$$

$$\frac{dx(t)}{dt} = -\frac{\mathrm{a}\sin(t)(sin^2(t) + 2cos^2(t) + 1)}{(sin^2(t) + 1)^2} \quad \text{[A17]}$$

And we get

$$V_{gap} = \frac{\sqrt{\left(\mathrm{a}(\sin^4(t) + \sin^2(t) + (\sin^2(t) - 1)\cos^2(t))\right)^2 + \left(\mathrm{a}\sin(t)(sin^2(t) + 2cos^2(t) + 1)\right)^2}}{(sin^2(t) + 1)^2} \quad \text{[A18]}$$

[5] Seen as the grey dots possibly not visible in paper print.

A2 Efficiency and losses

The power that has ended up as useful hydraulic power in the flow, P_{hyd}, is described by

$$P_{hyd} = \rho g Q H \qquad \text{[A19]}$$

Where ρ [kg/m^3] is the density of the water, g is gravitational acceleration [m/s^2], Q [m^3/s] is the flow through the section, H [m] is the head measured as the difference in specific hydraulic energy between inlet and outlet of the section. This power is supplied by the pumping unit, but the unit must also supply the power to cover all the losses. These losses are reduction in the head due to losses in the flow, like friction and vortices generated and eventually dissipated, and leakages through the machine which reduce the delivery of water to the system by the unit. If we call the power the unit must deliver to the water P_{unit}, we can write

$$P_{unit} = P_{hyd} + P_{losses} \qquad \text{[A20]}$$

Where P_{losses} are the sum of all such losses. Driving the machine is mechanical power, acting as a torque T [Nm] maintaining an angular velocity ω [rad/s]. If no additional torque is opposing the rotation all the mechanical power is perfectly transformed to the power delivered by the unit to the water. This is however not the case, as the rotating parts will feel that different boundaries are trying to limit the movement by acting with a torque on the parts. If we aggregate all these torques into a single term and call them $T_{boundaries}$ we can write

$$P_{mech} = P_{unit} + \omega T_{boundaries} \qquad \text{[A21]}$$

The efficiency of this energy conversion will be

$$\eta = \frac{P_{hyd}}{P_{mech}} = \frac{\rho g Q H}{P_{hyd} + P_{losses} + \omega T_{boundaries}} \qquad \text{[A22]}$$

To be able to find this efficiency we must describe the leakages, losses in head, and the torques acting on the unit from the boundaries. We will be starting with the flow losses.

A2.1 Flow losses

The flow through the system is the flow displaced by the rotors of the unit, $Q_{displaced}$, plus the flow through the gaps close to the rotors and in between the rotors, Q_{gaps}.

$$Q = Q_{displaced} + Q_{gaps} = 2A_{lobe}Z_{lobe}N_{lobes}n_{rps} + Q_{gaps} \qquad \text{[A23]}$$

Where A_{lobe} is the area of the waterfilled part of the lobes, Z_{lobe} is the height of the lobes, N_{lobes} is the number of lobes pr rotor, n_{rps} is the number of revolutions pr second.

The gap flow occurs between the rotors and casing, Q_{rc}; between the two rotors, Q_{rr}; between the ends of the rotors, Q_{ends}:

$$Q_{gaps} = Q_{rC} + Q_{rr} + Q_{ends} \qquad \text{[A24]}$$

Note that the gap flow has a positive sign in the same direction as the displaced flow. Individual investigations of the gap flows will reveal if the flow is in this direction or not. Caution must be made if the model is intended applied to generating mode as well, carefully monitoring the signs.

A2.2 Q_{rc} and Q_{rr}

Q_{rc} and Q_{rr} is assumed to be estimated from the concept of pressure driven Couette flows where the velocity profile is the superposition of a linear profile due to the velocity difference between the two solid surface boundaries and a parabolic profile due to the pressure difference. The basic concept of the pressure driven Couette flow is developed using two parallel flat plates, but for small gaps it is frequently used as an approximation for non-flat plates as well.

A2.2.1 Qrc

The working sketch for the flow through the rotor-casing gap is seen schematically in Figure 35.

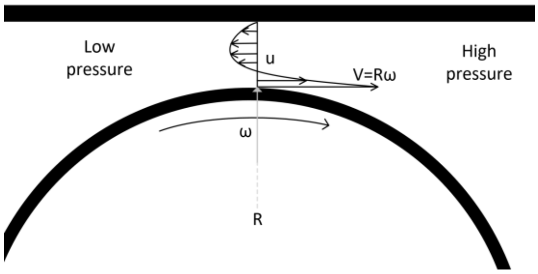

Figure 35: Sketch of rotor-casing gap flow

The velocity profile for this kind of flow is given by (y=0 at rotor and y=h at casing)

$$u = \frac{1}{2\mu}\frac{\partial P}{\partial x}(y^2 - hy) - \frac{Vy}{h} + V \quad \text{[A25]}$$

Where V (m/s) is the velocity of the moving surface, h [m] is the gap, y [m] is the position in the gap, dP/dx [pa/m] is the pressure gradient over the gap (increasing pressure to the right), μ [kg/ms] is the dynamic viscosity. Integrating this over the gap (h) and multiplying with the lobe height gives the flow through the gap, Qrc, which for the casing rotor gap becomes

$$Q_{rc} = Q_{Vrel} + Q_{dP} = Z_{lobe}\frac{Vh}{2} - Z_{lobe}\frac{1}{12\mu}\frac{\partial P}{\partial x}h^3 \quad \text{[A26]}$$

Where Q_{Vrel} is the flow driven by the relative motion between the rotor and casing, Q_{dP} is the flow driven by the pressure gradient. These terms are equal each of the terms in the final right-hand side, respectively. One remark must be made on the pressure gradient in the pressure driven Couette flow case: The pressure gradient is the result of friction losses in the flow, and the gap between the casing and rotor is very short and the flow is accelerated from the high-pressure side to the low-pressure side. Using the pressure difference over the gap divided by some distance will give a far to big velocity component, yet we will have use for the velocity profile in the later work and we will therefor use a different approach to find a value for $\partial P/\partial x$. Using the energy equation from high to low pressure side including a loss coefficient we can find the average velocity (for the parabolic component) through the gap as

$$V_{avg,dP} = -C\sqrt{2gH} \quad \text{[A27]}$$

Where C is a coefficient between 0 and 1, 1 indicating the maximum velocity possible (Torricelli theorem). This coefficient has been found using the actual flow found in 2D CFD simulations of a positive displacement machine at very low rotational speeds, which will capture the flow due to the pressure driven component only. The value was approximated to be C=0,65.

The flow is the velocity multiplied with the cross sectional area, and setting this equal to the pressure gradient flow from the Couette flow field we can find the pressure gradient[6]

$$Q_{dP} = V_{avg,dP} Z_{lobe} h = -C\sqrt{2gH} Z_{lobe} h = -\frac{Z_{lobe}}{12\mu}\frac{\partial P}{\partial x} h^3 \quad \text{[A28]}$$

And we find the pressure gradient as

$$\frac{\partial P}{\partial x} = \frac{-12\mu V_{avg,dP}}{h^2} = \frac{12\mu C\sqrt{2gH}}{h^2} \quad \text{[A29]}$$

The flow in the gap becomes

$$Q_{rc} = Z_{lobe}\left(\frac{V}{2} - C\sqrt{2gH}\right)h \quad \text{[A30]}$$

A2.2.2 Q_{rr}

The working sketch for the flow through the gap between the rotors are seen in Figure 36.

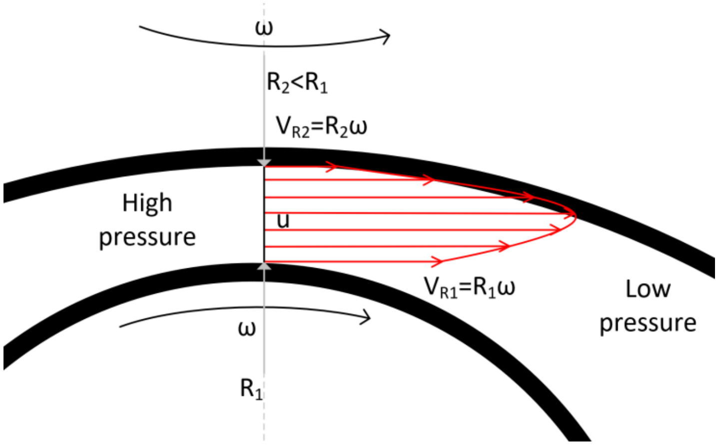

Figure 36: Sketch of rotor-rotor gap flow

The velocity profile is generally described by

$$u = \frac{1}{2\mu}\frac{\partial P}{\partial x} y^2 + Cy + B \quad \text{[A31]}$$

[6] We don’t need the pressure gradient for the case of the flow calculation, but we’ll need this later when assessing the torques

Where C and B are coefficients determined from boundary conditions. If we look at the case when the smallest gap is at the largest radii of rotor 1, the velocity profile is described by

$$u = \frac{1}{2\mu}\frac{\partial P}{\partial x}y^2 + Cy + B \tag{A32}$$

The coefficients are determined from boundary conditions and if we look at the case when the smallest gap is at the largest radii of rotor 1, and the velocity profile is described by

$$u = \frac{1}{2\mu}\frac{\partial P}{\partial x}(y^2 - hy) + \frac{V_{R/2} - V_R}{h}y + V_R \tag{A33}$$

Where y=0 is on the surface of the left rotor. Here, the rotor surface is in the opposite direction than at the gap, it is in the same direction as the positive flow. To be able to express the velocity as angular velocity times the radius complying to the positive flow definition we have to change the sign; i.e. $V_R = -\omega R$, $V_{R/2} = -\omega R/2$.

At half cycle rotor 1 is lagging and the velocity profile is described by

$$u = \frac{1}{2\mu}\frac{\partial P}{\partial x}(y^2 - hy) + \frac{-\omega R/2 + \omega R}{h}y - \omega R = \frac{1}{2\mu}\frac{\partial P}{\partial x}(y^2 - hy) + \frac{\omega R}{2h}y - \omega R \tag{A34}$$

We see that the term linked to the pressure gradient stays unchanged, but the term linked to the rotor velocities change sign as well as the constant being the smaller velocity $V_{R/2}$.

Integrating these velocity profiles gives the same result, and we therefore assume the flow to be constant and independent og the gap position; over the gap gives the flow when integrating over the rotor height.

$$Q = Z_{lobe}\left(-\frac{1}{12\mu}\frac{\partial P}{\partial x}h^3 + (V_{R2} + V_{R1})\frac{h}{2}\right) \tag{A35}$$

Which, because the sum of the rotor peripheral velocities always equals two times the velocity at pitch radius r=κR, simplifies to

$$Q_{rr} = Q_{Vrel} + Q_{dP} = -Z_{lobe}\omega\kappa Rh - Z_{lobe}\frac{1}{12\mu}\frac{\partial P}{\partial x}h^3 \tag{A36}$$

The pressure gradient is giving the same difficulty as was the case for the rotor-casing gap. Adding to the difficulty, the difference in head across this gap is actually bigger than what is represented by the head H, simply because the pressure increases and decreases on the high pressure and low-pressure sides, respectively, due to the displacing action. Faster rotational speed displaces the same volume in a smaller time and requires a higher pressure increase than the displacement at lower rotational speed. The head increase is assumed to be proportional with the square of the difference in rotor tip and the smallest rotor diameter velocity, as the difference in these velocities represent the displacing action there the tip of one rotor is hunting the through of the other rotor. Since the rotors share the rotational speed this term is due to the difference in peripheral speed because of rotor radius difference at the gap location, which is described

$$\Delta H = \frac{(\Delta u)^2}{2g} = \frac{(\omega \Delta R)^2}{2g} \quad \text{[A37]}$$

This difference $\omega\Delta R$ is what is resulting in the gap moving in the y-direction, ref the lemniscate trace. This makes it possible for us to link the increase in head to the gap velocity in the y direction by stating

$$\omega \Delta R = \frac{dy}{dt} \quad \text{[A38]}$$

When the gap is moving up, i.e. a positive velocity in the axial direction, the gap has started at a position which is one of the extreme locations, either fully to the left or fully to the right. Moving one quarter the lemniscate cycle shifts the gap position from either right or left. This is one cycle of displacement/replacement, and finding the average value of the magnitude of the gap velocity in the axial direction is used as the average value for the pressure increase/decrease due to displacement/replacement action, this can be done by integrating the absolute value of Eq. [A16], the axial velocity of the lemniscate trace. Integrating the velocity gives the position, so we can evaluate the integral directly by viewing the absolute distance the gap has travelled as two times the quarter lemniscate cycle distance of Eq. [A14]. This distance Δy, becomes

$$\Delta y = \frac{\sqrt{2}a}{3} = \frac{\sqrt{2}R}{12} \quad \text{[A39]}$$

The time for this travel is

$$\Delta t = \frac{\pi/4}{\omega} \quad \text{[A40]}$$

$$\omega \Delta R = \frac{dy}{dt} = \frac{\sqrt{2}R\omega}{3\pi} \approx 0{,}15R\omega \quad \text{[A41]}$$

Using the energy equation between a point in front of the gap with a pressure P^+ and the addition due to displacement and velocity V to a point behind the gap with the same velocity and pressure P^- minus the pressure due to replacement (negative displacement) and using the head loss linked to the pressure gradient described by the average gap velocity (Eq. [A29]) we can write

$$H^+ - \frac{1}{2g}\omega|\omega|(0{,}15R)^2 = H^- + \frac{1}{2g}\omega|\omega|(0{,}15R)^2 + \frac{1}{2g}V_{gap,dP}^2 - \frac{4L}{\rho g}\frac{\partial P}{\partial x} \quad \text{[A42]}$$

$$\frac{1}{2g}V_{gap,dP}^2 = H - \frac{0{,}045}{g}\frac{\omega|\omega|R^2}{2} + \frac{4L}{\rho g}\frac{\partial P}{\partial x} \quad \text{[A43]}$$

$$V_{gap,dP} = \sqrt{2gH + \frac{8L}{\rho}\frac{\partial P}{\partial x} - 0{,}045\omega|\omega|R^2} \quad \text{[A44]}$$

Where the sign of the angular velocity is kept rather than using the square to enable generating mode analysis at a later point. This investigation was in pump mode, where the displacing action gives and additional pressure at the high-pressure side and a reduced pressure at the low-pressure side. In turbine mode the pressure increase/decrease due to displacing action shifts position and possibly reverses the flow, as well as the sign for ω shifting, it is defined as positive in turbine mode.

We use the same methodology for the rotor-rotor gap by using the 2D CFD results at hand to find the pressure driven leakage flow component and linking this via a new coefficient C multiplied with the maximum theoretical velocity due to the head H. For the rotor-rotor gap the approximation of the coefficient resulted in C=0,3. Eq. [A29] is used to find the pressure gradient due to the friction in the gap flow.

$$V_{gap,dP} = \sqrt{2gH + \frac{8L}{\rho}\frac{\partial P}{\partial x} - 0{,}045\omega|\omega|R^2} \qquad \text{[A45]}$$

Summing up, the flow through the rotor-rotor gap, Qrr, is described by

$$Q_{rr} = -Z_{lobe}\omega\kappa Rh + Z_{lobe}h\sqrt{2gH + \frac{8L}{\rho}\frac{\partial P}{\partial x} - 0{,}045\omega|\omega|R^2} \qquad \text{[A46]}$$

A2.2.3 Q_{ends}

The end gaps have a pressure gradient forcing the flow, as well a rotation of the lobes which due to a pumping plate effect will move water in the direction of the peripheral direction of the rotors and adding a radial component where there is no casing limiting the radial component of the flow. If we assume that the axial component of the peripheral rotor velocity is representing the boundary condition for a Couette-like flow in the gap, we can integrate the peripheral component multiplied with the cosine of the angular position of the lobe over the an angle which from pi/2 to -pi/2 and from r=0 to r=R, Dividing by the area of this half disc, we get an average value for the component of the peripheral velocity in the axial direction[7]. Multiplying with the gap cross section we get the flow. The working sketch for this is seen below.

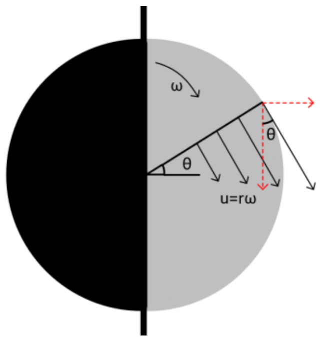

Figure 37: Working sketch for the end gap rotational flow analysis

The average velocity in axial direction is

[7] The continuity equation is violated applying this as it is analysed as a steady state problem, but the real problem is periodic and will not comply to a steady state continuity equation neither.

$$U_{average} = \frac{2}{\pi R^2} \iint_{r=0,\theta=\pi/2}^{r=\kappa R,\theta=-\pi/2} r\omega\, cos\theta r dr d\theta = -\frac{2}{\pi\kappa^2 R^2}\frac{2}{3}\omega\kappa^3 R^3 = -\frac{4}{3\pi}\omega\kappa R \quad \text{[A47]}$$

For four equal gaps we then have

$$Q_{ends,rotation} = U_{average}A = -\frac{4}{3\pi}\omega\kappa R \cdot 4h\kappa R = -\frac{16}{3\pi}\omega\kappa^2 R^2 h \quad \text{[A48]}$$

The pressure at the ends is acting over each side of the half circle. Working sketch for this is seen below.

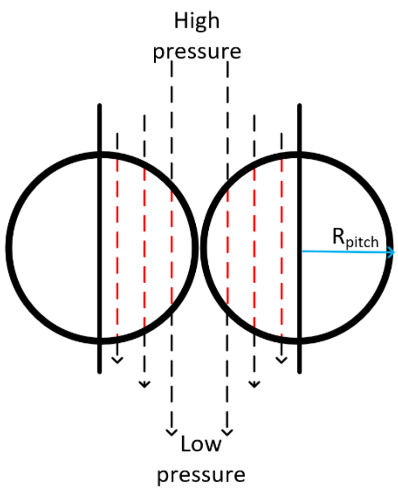

Figure 38: Working sketch for the end gap pressure driven leakage flow analysis

The dashed arrows are indicating velocity vectors and streamlines, their length not representing actual magnitude but initial qualitative estimation. The red part is where the flow passes through the gap, clearly a longer distance close to the rotation axis of the lobes than closer to the centre.

Using the energy equation along a streamline from high pressure/no velocity to low pressure/high velocity side including pressure gradient due to friction and loss of all gap velocity kinetic energy we can write

$$H^+ - H^- = H = \frac{1}{\rho g}\frac{\partial P}{\partial x}dx + \frac{V^2}{2g} = \frac{1}{\rho g}\frac{\partial P}{\partial x}dx + \frac{1}{2gh^2}\left(\frac{dQ}{dr}\right)^2 \quad \text{[A49]}$$

Assuming that we are working with a flow between two fixed flat plates with a pressure gradient we are back to the Couette flow assumption with a pressure gradient and no moving plate. The link between the flow and the pressure gradient is thus

$$\frac{dQ}{dr} = \int_{y=0}^{y=h} u dy = \frac{1}{2\mu}\frac{\partial P}{\partial x}\int_{y=0}^{y=h}(y^2 - hy)dy = -\frac{1}{12\mu}\frac{\partial P}{\partial x}h^3 \quad \text{[A50]}$$

Substituting the pressure gradient back into the energy equation we get a second order equation.

$$\frac{1}{2}\left(\frac{dQ}{dr}\right)^2 - \frac{12\mu}{\rho h}\frac{dQ}{dr}dx - gh^2H = 0 \qquad \text{[A51]}$$

Which solves as

$$\frac{dQ}{dr} = \frac{12\mu}{\rho h}dx \pm \sqrt{\left(\frac{12\mu}{\rho h}dx\right)^2 + 2gh^2H} \qquad \text{[A52]}$$

If H=0, there should be no leakage flow. Investigating the above equation, we see that this is the case when using the negative sign. So,

$$\frac{dQ}{dr} = \frac{12\mu}{\rho h}dx - \sqrt{\left(\frac{12\mu}{\rho h}dx\right)^2 + 2gh^2H} \qquad \text{[A53]}$$

For us, dx is not an infinitesimal small length, but the distance from front to back og the rotors, the red dashed lines in the work sketch. Expressing this using the radial position we can substitute

$$dx = 2\sqrt{(\kappa R)^2 - r^2} \qquad \text{[A54]}$$

And get

$$\frac{dQ}{dr} = \frac{24\mu}{\rho h}\sqrt{(\kappa R)^2 - r^2} - \sqrt{\left(\frac{24\mu}{\rho h}\right)^2 (\kappa R)^2 + 2gh^2H - \left(\frac{24\mu}{\rho h}\right)^2 r^2} \qquad \text{[A55]}$$

Integrating dQ/dr from r=0 to r=κR:

$$Q = \frac{24\mu}{\rho h}\frac{\pi(\kappa R)^2}{4} - \frac{24\mu}{\rho h}\int \sqrt{(\kappa R)^2 + \frac{2gh^2H}{\left(\frac{24\mu}{\rho h}\right)^2} - r^2}\, dr \qquad \text{[A56]}$$

And there's four ends like this, so we have to multiply with four to get the total end gap leakage due to the pressure gradient

$$Q_{ends,dP} = \frac{24\mu\pi(\kappa R)^2}{\rho h} - \frac{48\mu}{\rho h}\left(\kappa R\sqrt{\frac{2gh^4H\rho^2}{(24\mu)^2}} + \left((\kappa R)^2 + \frac{2gh^4H\rho^2}{(24\mu)^2}\right) atan\frac{\kappa R\frac{24\mu}{\rho h}}{\sqrt{2gh^2H}}\right) \qquad \text{[A57]}$$

The end flow will be the sum of the pressure gradient part and the rotational part;

$$Q_{ends} = Q_{ends,rotation} + Q_{ends,dP} \qquad \text{[A58]}$$

A2.3 Torques

The torques acting on the rotors opposing the movements are due to the shear forces originating from velocity gradients at rotor boundaries. These are in the gaps as well Torques are found by multiplying the forces with the radii at which they act, thus finding the forces is key.

$$T_{boundaries} = T_{rc} + T_{rr} + T_{gap} = F_{rc}R_{rc} + F_{rr}R_{rr} + T_{gap} \quad \text{[A59]}$$

A2.3.1 T_{rc}

The shear force acting on the rotor in the gap between the rotor and casing is found by differentiation of the gap velocity profile evaluated at the rotor wall, multiplied by viscosity and the area on which it acts.

$$\tau_w = \mu \frac{\partial u}{\partial y}\bigg|_{y=h} = \mu\left(\frac{V}{h} + \frac{1}{2\mu}\frac{\partial P}{\partial x}h\right) = \mu\left(\frac{\omega R}{h} + \frac{6C\sqrt{2gH}}{h}\right) \quad \text{[A60]}$$

When using the relation between pressure gradient and velocity we found when working with the gap flow. This is the shear at the smallest gap between rotor and casing. Obviously, the shear is smaller at other parts of the lobe ends, but using this maximum value we can adjust later. We must also multiply with the area to find the force. Using one sixth of the circumference (for a three lobe rotor), we overestimate the area where the shear acts (since the lobes are rounded), and using a factor C_{Trc} we can adjust both these assumptions, and that we use the maximum shear value, and multiplying with the entire rotor radius.

$$T_{rc} = R\frac{2\pi R}{6}Z_{lobe}C_{Trc}\tau_w = \frac{\pi R^2}{3}Z_{lobe}C_{Trc}\mu\left(-\frac{\omega R}{h} + \frac{6C\sqrt{2gH}}{h}\right) \quad \text{[A61]}$$

A2.3.2 T_{rr}

Same principle as for the gap, but different velocity profile and a different radius. Two key moments; when one rotor is pulling the other by shear, and when the other is doing the same, $1/12^{th}$ rotation later. The shear changes sign due to changing the lag/lead. At lead the shear is biggest and negative, at lag it is smallest and positive.

At the start or end of the cycle, "our" rotor in leading, and the velocity profile is described by Eq. [A33]

The gradient at the wall of our rotor is

$$\frac{du}{dy} = -\frac{1}{2\mu}\frac{\partial P}{\partial x}h + \frac{V_{R/2} - V_R}{h} = -\frac{1}{2\mu}\frac{\partial P}{\partial x}h - \frac{V_R - V_{R/2}}{h} \quad \text{[A62]}$$

At half cycle our rotor is lagging and the velocity profile is described by Eq. [A34], and the gradient at the wall of the rotor is

$$\frac{du}{dy} = -\frac{1}{2\mu}\frac{\partial P}{\partial x}h + \frac{V_R - V_{R/2}}{h} \quad \text{[A63]}$$

So, we see that the term linked to the pressure gradient stays unchanged, but the term linked to the rotor velocities change sign. The velocity gradient has the same magnitude but with different signs at these extreme occurrences, and due to the geometry and the constant angular velocity it is a fair assumption that the velocity gradient develops as a sinusoidal function of time and that the extreme occurrences represent the maximum values this. If we define t=0 when the left rotor has a lobe directly to the right side, we can write

$$\frac{du}{dy} = -\frac{1}{2\mu}\frac{\partial P}{\partial x}h - \frac{\omega\left|R - {}^{R}/_{2}\right|}{h}cos(3\omega t) = -\frac{1}{2\mu}\frac{\partial P}{\partial x}h - \frac{\omega R}{2h}cos(3\omega t) \quad \textbf{[A64]}$$

The force from the shear due to this velocity profile has a direction parallel to the rotor surface, $\vec{p} = C_x(t)\vec{x} + C_k(t)\vec{k}$, acting on an infinitesimal area dA at the gap location;

$$\vec{F} = \vec{p}\mu\frac{du}{dy}dA = \left(C_x(t)\vec{x} + C_k(t)\vec{k}\right)\mu\left(-\frac{1}{2\mu}\frac{\partial P}{\partial x}h - \frac{\omega R}{2h}cos(3\omega t)\right)dA \quad \textbf{[A65]}$$

Where $|\vec{p}| = 1$, and this links the components by $C_x = \sqrt{1 - C_k^2}$. We are looking for the torque contribution of the shear force to the rotation. This is described by

$$\vec{T} = \vec{r} \times \vec{F} \quad \textbf{[A66]}$$

Where the r-vector is the position vector from the axis of rotation to the gap position. How the position vector changes will require some additional analysis.

So as time changes, we have to map the lemniscate on to the geometry of one rotating lobe[8] to find the gap position on the lobe geometry and then find the tangent to that point. Doing this we can find the angle of the tangent and get the axial component, and subsequently the sideways component as well. The result is seen in Figure 39.

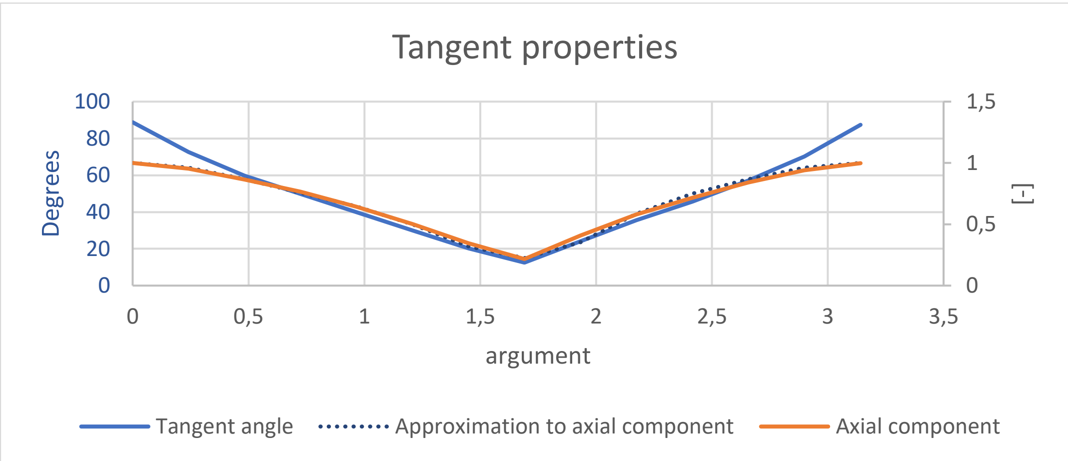

Figure 39: Tangent properties of lemniscate

The axial component is not very practical as it is showing a discontinuous behaviour. To be able to use this in the calculations an approximation is made, seen as the dashed line. The equation used is

$$C_k(t) = 0{,}7sin^2(t) + 0{,}4sin^4(t) - 0{,}3sin^8(t) - 0{,}2sin^{14}(t - 0{,}2)$$

Where t is the argument to the sine functions and must be adapted to match with the frequency of the rotor rotation. We now can use the Pythagorean theorem to find C_x, with no elaboration on this.

[8] Gap point using the lemniscate is more defined than just looking at two lobes and see where the gap is.

The torque can be written like

$$\vec{T} = \left(\left(\frac{3R}{4} + \frac{\mathrm{a} \cdot \cos(3\omega t)}{sin^2(3\omega t) + 1} \right) \vec{x} + \frac{\sqrt{2}\mathrm{a} \cdot \cos(3\omega t) \sin(3\omega t)}{sin^2(3\omega t) + 1} \vec{k} \right) \times \left(C_x(t)\vec{x} + C_k(t)\vec{k} \right) \mu \left(-\frac{1}{2\mu} \frac{\partial P}{\partial x} h - \frac{\omega R}{2h} cos(3\omega t) \right) dA \tag{A67}$$

Which becomes

$$T = \left(\left(\frac{3R}{4} + \frac{\mathrm{a} \cdot \cos(3\omega t)}{sin^2(3\omega t) + 1} \right) C_k(t)\vec{x}\vec{k} - C_x(t) \frac{\sqrt{2}\mathrm{a} \cdot \cos(3\omega t) \sin(3\omega t)}{sin^2(3\omega t) + 1} \vec{x}\vec{k} \right) \mu \left(-\frac{1}{2\mu} \frac{\partial P}{\partial x} h - \frac{\omega R}{2h} cos(3\omega t) \right) dA \tag{A68}$$

We have to describe the torque acting on the rotor for an entire cycle of the periodic behaviour of the machine, and integrating this means we have to substitute the differential area with a relation dependent on differential time. This relation is

$$dA = Z_{lobe} V_{gap} dt \tag{A69}$$

The average torque is obtained substituting Eq. [A69] into Eq. [A68], integrating it over the time for one period and dividing by the time for one period. The gap velocity V_{gap} is known from Eq. [A17]

$$T_{rr} = \frac{1}{2\pi/_{\omega}} \int_{t=0}^{t=2\pi/_{\omega}} \left(\left(\frac{3R}{4} + \frac{\mathrm{a} \cdot \cos(3\omega t)}{sin^2(3\omega t) + 1} \right) C_k(t)\vec{x}\vec{k} - C_x(t) \frac{\sqrt{2}\mathrm{a} \cdot \cos(3\omega t) \sin(3\omega t)}{sin^2(3\omega t) + 1} \vec{x}\vec{k} \right) \mu \left(-\frac{1}{2\mu} \frac{\partial P}{\partial x} h - \frac{\omega R}{2h} cos(3\omega t) \right) Z_{lobe} V_{gap} dt \tag{A70}$$

We have to work on this numerically due to the complexity of the torque equation, and the the torque as a function of time, the integral of the torque and the average torque value are seen in Figure 40 below.

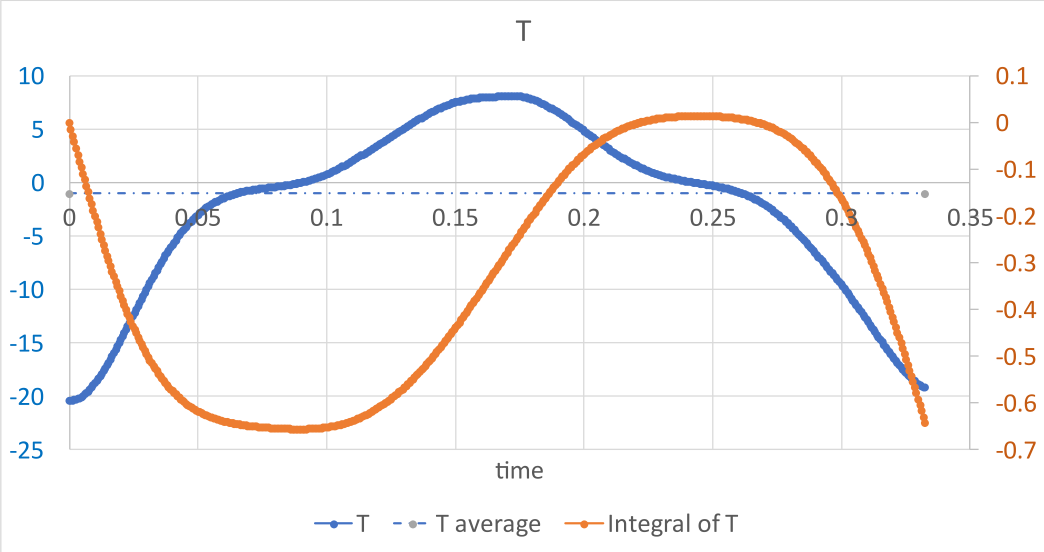

Figure 40: Torque characteristics of one displacement cycle due to gap flow characteristics (example, will vary with operating conditions)

The result shows that in this case the net torque (average value) is small and negative, meaning it tries to slow the rotor down. This is in line which what is expected, as the pressure gradient will drive flow through the gap always giving a torque contributing to the rotating motion, but the linear velocity profile in the gap due to the rotor rotation will oscillate between negative and positive values but the negative values are given more weight due to occurring at higher radius, giving a net negative contribution to the torque. This will of course be subject to rotational speeds and gap size, so the torques will change due to this and this is included in the analysis.

A2.3.3 Torque in the rotor ends

The Torque in the rotor ends are found based on the velocity profile as a combination of a linear velocity profile in the circumferential direction ($\vec{e}_\theta$) due to the rotating disc the end represent, and a parabolic velocity profile in the main flow direction ($\vec{j}$) because of leakage due to the pressure difference over the rotor. The velocity gradient will define the shear force vector, as defined below

$$d\vec{F} = \mu\frac{d\vec{u}}{dy}dA = \mu\left(-\frac{r\omega}{h}\vec{e}_\theta + \frac{1}{2\mu}\frac{\partial P}{\partial x}h\vec{j}\right)rd\theta dr$$
$$= \mu\left(-\frac{r\omega}{h}\vec{e}_\theta + \frac{1}{2\mu}\frac{\partial P}{\partial x}h(\vec{e}_\theta cos\theta + \vec{e}_r sin\theta)\right)rd\theta dr \quad \text{[A71]}$$

Substituting back into Eq. [A71] and finding the torque as the cross product of position vector and shear force vector we get

$$d\vec{T} = \vec{r}\times d\vec{F} = r\vec{e}_r \times \mu\left(-\frac{r\omega}{h}\vec{e}_\theta + \frac{1}{2\mu}\frac{\partial P}{\partial x}h(\vec{e}_\theta cos\theta + \vec{e}_r sin\theta)\right)rd\theta dr$$
$$= r^2\mu\left(-\frac{r\omega}{h} + \frac{1}{2\mu}\frac{\partial P}{\partial x}hcos\theta\right)\vec{k}d\theta dr \quad \text{[A72]}$$

The integration of this to the torque acting on the entire surface is performed in two parts, where the first part is integrated over the entire surface (r=0 to r=κR, θ=0 to θ=2π) as it is the part related to the relative velocity between the rotating part (disc) and the floor of the rotor casing. The other integral is performed similar to the leakage as this is linked to the velocity gradient of this leakage flow, i.e from r=0 to r=κR, θ= π/2 to θ=-π/2.

$$T = \int dT = -\frac{\mu\omega}{h}\iint_{r=0,\theta=0}^{r=\kappa R,\theta=2\pi} r^3 d\theta dr + \iint_{r=0,\theta=-\pi/2}^{r=\kappa R,\theta=\pi/2} r^2\left(\frac{1}{2}\frac{\partial P}{\partial x}h\cos\theta\right)d\theta dr \quad \text{[A73]}$$

Executing the first integral we get

$$T = -\frac{\pi\mu(\kappa R)^4\omega}{2h} + \frac{h}{2}\iint_{r=0,\theta=-\pi/2}^{r=\kappa R,\theta=\pi/2} r^2\frac{\partial P}{\partial x}\cos\theta d\theta dr \quad \text{[A74]}$$

The pressure gradient is linked to the leakage flow which we found for the end gap leakage flow section

$$\frac{\partial P}{\partial x} = -\frac{12\mu}{h^3}\frac{dQ}{dr} = -\frac{12\mu}{h^3}\left(\frac{24\mu}{\rho h}\sqrt{(\kappa R)^2 - r^2} - \sqrt{\left(\frac{24\mu}{\rho h}\right)^2(\kappa R)^2 + 2gh^2H - \left(\frac{24\mu}{\rho h}\right)^2 r^2}\right) \quad \text{[A75]}$$

Substituting into Eq. [A74] we get

$$\frac{h}{2}\iint_{r=0,\theta=-\pi/2}^{r=\kappa R,\theta=\pi/2} r^2\frac{\partial P}{\partial x}\cos\theta d\theta dr = -\frac{6\mu}{h^2}\iint_{r=0,\theta=-\pi/2}^{r=\kappa R,\theta=\pi/2} r^2\left(\frac{24\mu}{\rho h}\sqrt{(\kappa R)^2 - r^2}\right)\cos\theta d\theta dr + \frac{6\mu}{h^2}\iint_{r=0,\theta=-\pi/2}^{r=\kappa R,\theta=\pi/2} r^2\left(\sqrt{\left(\frac{24\mu}{\rho h}\right)^2(\kappa R)^2 + 2gh^2H - \left(\frac{24\mu}{\rho h}\right)^2 r^2}\right)\cos\theta d\theta dr \quad \text{[A76]}$$

Looking at the first integral separately we get

$$-\frac{6\mu}{h^2}\iint_{r=0,\theta=-\pi/2}^{r=\kappa R,\theta=\pi/2} \frac{24\mu}{\rho h}\left(r^2\sqrt{(\kappa R)^2 - r^2}\right)\cos\theta d\theta dr = -\frac{288\mu^2}{\rho h^3}\int_{r=0}^{r=\kappa R} r^2\left(\sqrt{(\kappa R)^2 - r^2}\right)dr = -\frac{288\mu^2}{\rho h^3}\frac{1}{16}\pi\frac{(\kappa R)^{9/2}}{\sqrt{\kappa R}} = -\frac{18\mu^2\pi(\kappa R)^4}{\rho h^3} \quad \text{[A77]}$$

Looking at the second integral separately we get

$$\frac{6\mu}{h^2}\iint_{r=0,\theta=-\pi/2}^{r=\kappa R,\theta=\pi/2} r^2\left(\sqrt{\left(\frac{24\mu}{\rho h}\right)^2(\kappa R)^2+2gh^2H-\left(\frac{24\mu}{\rho h}\right)^2 r^2}\right)cos\theta d\theta dr$$
$$=\frac{12\mu}{h^2}\frac{24\mu}{\rho h}\int_{r=0}^{r=\kappa R} r^2\left(\sqrt{(\kappa R)^2+\frac{2gh^4H\rho^2}{(24\mu)^2}-r^2}\right)dr$$
$$=\frac{288\mu^2}{\rho h^3}\int_{r=0}^{r=\kappa R} r^2\left(\sqrt{A^2+B^2-r^2}\right)dr \quad \text{[A78]}$$

Where the constant A is defined for simplicity as

$$A^2+B^2=\left((\kappa R)^2+\frac{2gh^4H\rho^2}{(24\mu)^2}\right) \quad \text{[A79]}$$

Executing the integral we get

$$\frac{288\mu^2}{\rho h^3}\int_{r=0}^{r=\kappa R} r^2\left(\sqrt{A^2+B^2-r^2}\right)dr$$
$$=\frac{288\mu^2}{\rho h^3}\frac{1}{8}\left(AB(A^2-B^2)+(A^2+B^2)^2 sin^{-1}\left(\frac{A}{\sqrt{A^2+B^2}}\right)\right)= \quad \text{[A80]}$$

$$\frac{36\mu^2}{\rho h^3}\left(\kappa R\sqrt{\frac{2gh^4H\rho^2}{(24\mu)^2}}\left((\kappa R)^2-\frac{2gh^4H\rho^2}{(24\mu)^2}\right)\right.$$
$$\left.+\left((\kappa R)^2+\frac{2gh^4H\rho^2}{(24\mu)^2}\right)^2 sin^{-1}\left(\frac{\kappa R}{\sqrt{(\kappa R)^2+\frac{2gh^4H\rho^2}{(24\mu)^2}}}\right)\right)$$

Trying to sum up this without making it too difficult for the eye, the torque is

$$T_{ends}=-\frac{2\pi\mu(\kappa R)^4\omega}{4h}-\frac{36\mu^2(\kappa R)^4}{\rho h^3}-LHS\ Eq.[\text{A80}] \quad \text{[A81]}$$

A2.3.4 Loss of rotation

The volume of water enclosed by the lobe geometry is given a solid body rotation which it didn't have prior to being "caught" by the lobes. The trapped water will also rotate due to the effect of the shear forces with the casing wall. In effect, the no-slip condition at the casing will determine that the absolute velocity here is zero, and that the rotation of the trapped water will be rotating in the opposite direction of the rotor rotation. The combined effect of these two rotations is giving a velocity profile along the radii between r=R/2 and r=R described by

$$u = -3\omega r + 4\omega\kappa R \quad \text{[A82]}$$

The water is entering the machine with no angular momentum and leaves with angular momentum according to the velocity above.

Angular momentum equation then tells us what the torque applied to the flow must be:

$$\vec{T} = \int (\vec{r} \times \vec{u})(\vec{u}_{rel} \cdot \vec{n})dA \quad \text{[A83]}$$

$$T = Z_{lobe} \int r(-3\omega r + 4\omega\kappa R)dr = \quad \text{[A84]}$$

$$Z_{lobe}\left((-\omega R^3 + 2\omega\kappa R^3) - \left(-\omega\left(\frac{R}{2}\right)^3 + 2\omega\kappa R\left(\frac{R}{2}\right)^2\right)\right) = Z_{lobe}\left(\frac{1}{4}\right)\omega R^3$$

This is contained within the flow, whereas if the internal rotation (the part due to no-slip at the casing wall) hadn't been initiated we would get

$$T = Z_{lobe} \int r(\omega r)dr = Z_{lobe}\left(\frac{\omega R^3}{3} - \frac{\omega\left(\frac{R}{2}\right)^3}{3}\right) = Z_{lobe}\frac{7\omega R^3}{24} \quad \text{[A85]}$$

This means that we should have gotten 7/24, but only got 6/24, 1/24 has been lost.

$$T_{l,rot} = Z_{lobe}\frac{\omega R^3}{24} \quad \text{[A86]}$$

The 6/24'ths is assumed to represent kinetic energy which is converted into pressure energy when it is stagnated on the surface of the oncoming opposing rotor.

A2.4 Head losses

In pipe flow, head losses are energy dissipation due to shear forces and vortices being initiated and driven by pressure, eventually the kinetic energy is dissipated and pressure is not recovered. This happens in the boundary layer close to walls, and at locations on the geometry that induce vortices. We have already made use of the velocity profiles and their gradients at the rotor surfaces to describe the torques acting on the rotors. Investigating the same velocity profiles at the fixed boundaries will give the head loss for the flow. The leakage flow through the rotor-casing gap is already assigned the full head loss as it is deducted from the flow as a leakage, the same goes for the end gaps leakage flows. The last part where the water is in contact with the fixed surface is the volume between the lobes which carry the theoretically displaced flow. The fixed casing no-slip boundary condition here will initiate a rotation of the water in this volume, and the shear forces at the fixed casing wall is a loss to the flow, described next.

A2.4.1 Head loss due to the rotation between lobes

The rotational velocity of the water between the lobes can be modelled as a solid body rotation and can be described by

$$u = -3\omega r + 4\omega\kappa R \quad \text{[A87]}$$

The shear force at the casing wall is the velocity gradient at the wall multiplied with the viscosity and the area

$$F = \mu \left.\frac{\partial u}{\partial y}\right|_{r=R} A = -3\omega\mu A \quad \text{[A88]}$$

Looking for the head due to the rotation of the loss we have to find

$$h_{L,rot} = \frac{F}{\rho g A} = -\frac{3\mu\omega}{\rho g} \quad \text{[A89]}$$

A2.4.2 Minor losses

Minor losses are linked to components and their operation and geometries, which we will assume have been covered by the analysis above, apart from one loss which is due the effect of the displaced water forming a jet in which kinetic energy is not recovered as pressure energy but is dissipated.

A2.4.3 Jet losses

The water is squeezed between the lobes where the lobes increase the pressure to more than the reservoir pressure hence acceleration the water towards the upper reservoir. The pressure by this squeezing action has been addressed before, when the rotor-rotor leakage flow were discussed. The analysis resulted in a gap velocity expression.

$$V_{gap,dP} = \sqrt{2gH + \frac{8L}{\rho}\frac{\partial P}{\partial x} - 0{,}045\omega|\omega|R^2} \quad \text{[A90]}$$

The last term under the root sign is due to the additional pressure of displacement action. This is the cause for the jet, so the jet velocity is

$$V_{jet} = \sqrt{0{,}045}\omega R \quad \text{[A91]}$$

If such a jet entered a large volume abruptly, as in a pipe leading straight to a reservoir, all the kinetic energy is lost, a loss coefficient equal to 1. However, the gap is not a sudden expansion but a more gradual one, and investigation of the lobe gradients show that at the gap there is an expansion of approximately one degree, which increases non-linearly through the centre region. The loss coefficient is difficult to assess, but as an indication an angle of 20 degrees and a gap-to-opening ration of 0.2 the loss coefficient is 0.3. For the purpose of this model we use C=0.1 as the loss coefficient. We get the head loss due to this water jet represented as

$$h_{L,jet} = C\frac{V_{jet}^2}{2g} = \frac{0{,}0045}{2g}(\omega R)^2 \qquad \text{[A92]}$$

The flow experiencing this loss is not the entire flow through the machine, but the flow carried by the jet. This makes it important to remember to weigh this loss with the flow of the jet relative to the flow of the machine, if this loss is subtracted from the head. Alternatively, the power loss due to this head loss can be added to the term P_{mech} in the denominator as a separate term.

$$P_{L,jet} = \rho g h_{L,jet} Q_{jet} = \rho g h_{L,jet} V_{jet} Z_{lobe} h \qquad \text{[A93]}$$

In turbine mode the displacement action is on the low pressure side, and CFD results indicates that a large eddy is formed near the gap rather than a jet. It's assumed here that even if the displacement action is resulting in two different root causes of head loss, their cause are described by the same potential forming and the mathematical application of this loss in turbine mode will be well described by Eq. [A93] as well.

A3 Summary

Applying all the leakages and losses and torques described in this document to Eq. [A22] the efficiency ends up being described by

$$\begin{aligned}\eta &= \frac{\rho g Q H}{P_{hyd} + P_{losses} + \omega T_{boundaries}} \\ &= \frac{(2Z_{lobe} n A_{wet} + Q_{rc} + Q_{rr} + Q_{ends})}{\rho g\left((2Z_{lobe} n A_{wet} + Q_{rc} + Q_{rr} + Q_{ends})(H - h_{L,rot})\right) - P_{L,jet} + 2\pi n(T_{rc} + T_{rr} + T_{ends} + T_{L,rot})}\end{aligned} \qquad \text{[A94]}$$

As a last-minute note, the rotor-rotor and rotor-casing gap flows have had constants calibrated by CFD results at very low rotational speeds, assumed to be representative for stand-still rotors. Other leakages/losses/torques may require calibration of assumptions/constants and should still be verified against other models. Ultimately the analytical model must be validated against experimental results.